Mon. Not. R. Astron. Soc. **295,** 877–898 (1998)

Semi-analytic modelling of galaxy evolution in the IR/submm range

Bruno Guiderdoni,[1] Eric Hivon,[2] François R. Bouchet[1] and Bruno Maffei[3]

[1]*Institut d'Astrophysique de Paris, CNRS, 98bis Boulevard Arago, F-75014 Paris, France*
[2]*Theoretical Astrophysics Center, Juliane Maries Vej 30, DK-2100 Copenhagen, Denmark*
[3]*Queen Mary and Westfield College, Mile End Road, London E1 4NS*

Accepted 1997 November 7. Received 1997 October 1; in original form 1997 July 28

ABSTRACT

This paper proposes a new semi-analytic modelling of galaxy properties in the IR/submm wavelength range, which is explicitly set in a cosmological framework. We start from a description of the non-dissipative and dissipative collapses of primordial perturbations, and add star formation, stellar evolution and feedback, as well as the absorption of starlight by dust and its re-emission in the IR and submm. This type of approach has had some success in reproducing the *optical* properties of galaxies. We hereafter propose a simple extension to the IR/submm range. The growth of structures is followed according to the standard cold dark matter model. We assume that star formation proceeds either in a 'quiescent' mode, e.g., as in discs, or in a 'burst' mode with 10 times shorter time-scales. In order to reproduce the current data on the evolution of the comoving cosmic star formation rate and gas densities, we need to introduce a mass fraction involved in the 'burst' mode strongly increasing with redshift, probably reflecting the increase of interaction and merging activity. We estimate the IR/submm luminosities of these 'mild starburst' and 'luminous UV/IR galaxies', and we explore how much star formation could be hidden in heavily extinguished, 'ultraluminous IR galaxies' by designing a family of evolutionary scenarios which are consistent with the current status of the 'cosmic constraints', as well as with the *IRAS* 60-μm luminosity function and faint counts, but with different high-z IR luminosity densities. However, these scenarios generate a cosmic infrared background whose spectrum falls within the $\pm 1\sigma$ range of the isotropic IR component detected by Puget et al. and revisited by Guiderdoni et al. We give predictions for the faint galaxy counts and redshift distributions at IR and submm wavelengths. The submm range is very sensitive to the details of the evolutionary scenarios. As a result, the ongoing and forthcoming observations with *ISO* and SCUBA (and later with *SIRTF*, SOFIA, *FIRST* and *PLANCK*) will put strong constraints on the evolution of galaxies at $z \sim 1$ and beyond.

Key words: galaxies: evolution – galaxies: formation – cosmology: theory – infrared: galaxies.

1 INTRODUCTION

This paper describes a new modelling of galaxy evolution in the infrared and submm wavelength ranges, which are now open to high-redshift exploration by the ongoing observations with *ISO* and SCUBA, and forthcoming facilities and experiments such as *SIRTF*, SOFIA, *FIRST* and *PLANCK*.

As a matter of fact, our knowledge of the early epochs of galaxies has recently increased, thanks to the richness and precision of the observational evidence obtained by UV/visible/near-infrared (NIR) surveys of high-redshift objects (Lilly et al. 1995; Cowie et al. 1996; Ellis et al. 1996; Steidel et al. 1996; Williams et al. 1996). The pattern of galaxy evolution which emerges from these data can be summarized as follows. (i) Faint galaxy counts show the presence of a large number of blue objects, well in excess of no-evolution expectations (Williams et al. 1996). (ii) These blue objects are 'sub-L^*' galaxies undergoing strong bursts of star formation (Ellis et al. 1996; Lilly et al. 1996). (iii) The

fraction of these blue objects with unclassified/peculiar morphologies showing signs of tidal interaction and merging (Abraham et al. 1996) increases from local samples to the *HST* high-resolution observations of the Medium Deep Survey (Griffiths et al. 1994) and Hubble Deep Field (HDF; Williams et al. 1996). (iv) The global star formation rate (SFR) of the Universe declined by a factor of about 10 since redshift $z \sim 1$ (Lilly et al. 1996; Madau et al. 1996; Connolly et al. 1997; Sawicki, Lin & Yee 1997). (v) Finally, this high SFR seems to be correlated to the decrease of the cold-gas comoving density associated with damped Lyman-α systems between $z = 2$ and 0 (Storrie-Lombardi, McMahon & Irwin 1996). These results nicely match a picture in which star formation in bursts triggered by interaction/merging consumes the gas content of galaxies as time goes on. It is common wisdom that such a qualitative scenario is expected within the paradigm of hierarchical growth of structures. The implementation of hierarchical galaxy formation in semi-analytic models quantitatively substantiates this view, and may further suggest that we have seen the bulk of star formation and understood the broad features of galaxy formation (Baugh et al. 1998).

However, it should be emphasized that this seemingly consistent view is entirely based on visible/NIR observations which probe only the rest-frame UV/visible light of high-z objects. The total amount of energy released by star formation should be estimated by summing up the UV/visible/NIR light of stellar populations directly escaping from galaxies, *and* the part which has been absorbed by dust and re-emitted in the IR/submm wavelength range. The corrections needed to account for optical extinction by dust are rather uncertain, and could easily induce an upward revision of the high-redshift SFR deduced from rest-frame UV/visible observations by factors of a few. Moreover, a significant fraction of star formation might be completely hidden in heavily extinguished galaxies which are missed by the above-mentioned surveys. Even for normal objects like spiral galaxies, the fraction of energy emitted in the IR can amount to 30 per cent of the optical, and this can increase to more than 95 per cent for ultraluminous starbursts. As a matter of fact, the IR/submm range might be more adequate than the optical for observing high-redshift, starburst galaxies, provided they are dusty. The rest-frame IR/submm spectrum of dust heated by a young stellar population peaks between 50 and 100 μm, pointing out the submm range as particularly relevant for the search of primeval, high-redshift galaxies.

At this time, we know very little about the 'optically dark' side of galaxy evolution. The *IRAS* satellite has given the first complete survey of far-infrared (FIR) galaxy properties, in four bands between 12 and 100 μm. Many studies have emphasized the wide variety of IR luminosities, from 'normal spirals' to 'mild starbursts', and finally to the 'luminous IR galaxies' (LIGs), mostly interacting systems, and the spectacular 'ultraluminous IR galaxies' (ULIGs), which are mergers (Clements et al. 1996b; Sanders & Mirabel 1996). Unfortunately, while we have learned from *IRAS* that about one-third of the bolometric luminosity of the local Universe is released in the IR/submm (Soifer & Neugebauer 1991), we know very little about galaxy evolution in this wavelength range. Faint galaxy counts and redshift surveys down to flux densities $S_\nu \sim 60$ mJy (at 60 μm) do not probe deeper than $z \sim 0.2$ (Ashby et al. 1996; Clements et al. 1996a). These surveys seem to show a strong luminosity and/or density evolution of *IRAS* sources, but it is difficult to extrapolate this trend to higher redshifts on a firm ground. In spite of its observational limits, *IRAS* has also revealed the existence of IRAS 10214 + 4724, a very peculiar, 'hyperluminous' galaxy at $z = 2.286$ (Rowan-Robinson et al. 1991a), although this object is probably affected by lensing (Eisenhardt et al. 1996). It is expected that the *ISO* satellite will complete and detail this picture, in a broader wavelength range from a few μm to 200 μm. Other projects, such as *SIRTF*, will give access to better sensitivity and imaging capabilities.

The properties of galaxies in the submm range are sensitive to the spectral characteristics of dust, especially its emissivity at large wavelengths which is not constrained by *IRAS* observations alone. With respect to the relative wealth of data in the FIR, the submm emission of galaxies is poorly known. The observational literature gathers the submm fluxes of only a few tens galaxies which have been measured from ground-based or aircraft-borne instruments. These observations are difficult, and some of the estimates of the amount of energy released in this range happen to be strongly discrepant (e.g. Chini et al. 1986; Stark et al. 1989; Eales, Wynn-Williams & Duncan 1989; Chini & Krügel 1993). However, the observational situation will soon evolve with the start of SCUBA operations (and later with SOFIA and especially *FIRST*). About 10 counterparts of radio galaxies and quasars have already been observed at submm/mm wavelengths (see, e.g., Hughes, Dunlop & Rawlings 1997, and references therein). Although their evolutionary status is not fully understood, these objects give a first flavour of the future deep surveys which will be achieved by forthcoming instruments.

Theoretical modelling is needed to optimize observational strategies and also to help assess the point source contribution of the forthcoming cosmic microwave background (CMB) satellites *MAP*, and especially *PLANCK*. These experiments aim at mapping the anisotropies of the submm/mm sky on scales well below the degree. On these scales, the separation of the various foregrounds and backgrounds which superimpose to the fluctuations of the CMB is more difficult than for the 7° field of view of the very successful *COBE*/DMR experiment. In the case of *PLANCK*, preliminary studies have shown that several thousands of galaxies should be detected at several wavelengths between 400 μm and 1 cm.

The epoch of galaxy formation can also be observed by its imprint on the background radiation which is produced by the line-of-sight accumulation of extragalactic sources. The search for the 'cosmic optical background' (COB) currently gives only upper limits. Nevertheless, the shallowing of the faint counts obtained in the HDF suggests that we are now close to convergence (Williams et al. 1996). Thus the lower limit to the COB obtained by summing up the contributions of faint galaxies is likely close to the real value. At longer wavelengths, the DIRBE instrument on *COBE* has given upper limits on the FIR background between 2 and 240 μm (Hauser 1995), while Puget et al. (1996) have discovered an isotropic component in the *COBE*/FIRAS residuals between 200 μm and 2 mm, which could be the long-sought 'cosmic infrared background' (CIB). The presence of this component is confirmed by a new analysis restricted to the

cleanest regions of the sky, where the foreground Galactic components are negligible (Guiderdoni et al. 1997). Such a detection seems to yield the first 'post-*IRAS*' constraint on the high-z evolution of galaxies in the IR/submm range, before the era of *ISO* results. Its level comparable to the above-mentioned estimate of the COB suggests that a significant fraction of the energy of young stars is absorbed by dust and released in the IR/submm.

The models which have been proposed to predict the faint counts and background radiation in the IR/submm can be classified as 'backward evolution' and 'forward evolution', following the good review by Lonsdale (1996). In the first class of models, the IR/submm luminosity function undergoes luminosity and/or number evolution which are simply parametrized as power laws of $(1+z)$ (e.g. Weedman 1990; Beichman & Helou 1991; Hacking & Soifer 1991; Oliver, Rowan-Robinson & Saunders 1992; Blain & Longair 1993a,b; Treyer & Silk 1993; Pearson & Rowan-Robinson 1996). These power laws are generally derived from fits of *IRAS* galaxy counts (which do not probe deeper than $z \simeq 0.2$). Then they are extrapolated up to redshifts of a few units. Unfortunately, various analyses of *IRAS* deep counts yield discrepant results at $S_{60} < 300$ mJy, and the issue of the evolution is very controversial (see, e.g., Bertin, Dennefeld & Moshir 1997 for a new analysis and discussion).

In the second class of models, the photometric evolution in the IR/submm is computed by implementing some of the involved physical processes. For instance, chemical evolution, which rules the amount of dust responsible for the IR/submm emission, is modelled in Wang (1991a,b) and Eales & Edmunds (1996, 1997). In addition to chemical evolution, the photometric evolution of stellar populations which heat the dust is modelled by Franceschini et al. (1991, 1994) and Fall, Charlot & Pei (1996). While the previous models assume a simple relation between the dust content and the heavy-element abundance of the gas, Dwek & Városi (1996) try to explicitly model the processes of dust formation and destruction. However, both classes of models assume that all galaxies form at the same redshift $z_{\rm for}$, and that there is no number evolution. The paradigm of the hierarchical growth of structures, however, implies that there is no clear-cut redshift $z_{\rm for}$, since galaxy formation is a continuous process. Only Blain & Longair (1993a,b) proposed a formalism to compute the redshift range of galaxy formation, in addition to chemical evolution.

A consistent approach to the early evolution of galaxies is particularly important for any attempt at predicting their submm properties. Fig. 1 shows *model* spectra of a luminous IR galaxy as it would be observed if placed at different redshifts. There is a wavelength range, between ~ 600 μm and ~ 4 mm, in which the distance effect is counterbalanced by the 'negative k-correction' due to the huge rest-frame emission maximum at ~ 100 μm. In this range, the apparent flux of galaxies depends weakly on redshift to the point that, evolution aside, a galaxy might be easier to detect at $z=5$ than at $z=0.5$! The observer-frame submm fluxes, faint galaxy counts and diffuse background of unresolved galaxies are consequently very sensitive to the early stages of galaxy evolution. Note that this particular wavelength range brackets the maximum of emission of the CMB.

The dissipative and non-dissipative processes ruling galaxy formation in dark matter haloes have been studied by

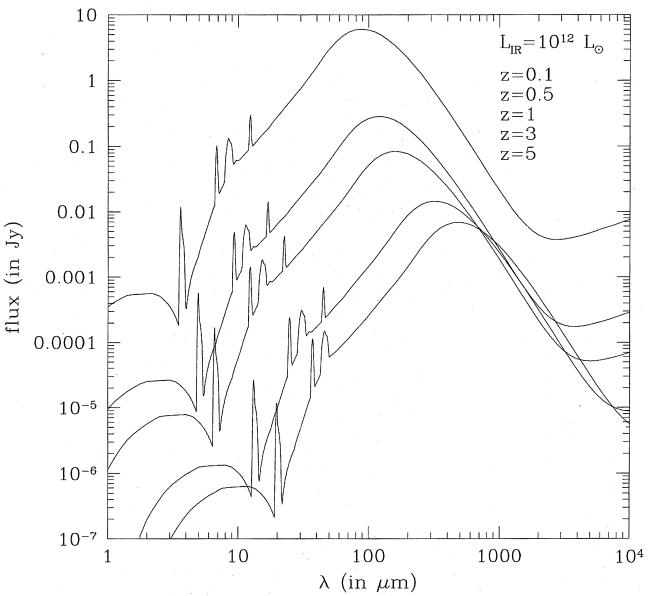

Figure 1. Observer-frame model spectra of a $L_{\rm IR}=10^{12}$ $L_\odot$ galaxy at increasing redshifts (from top to bottom), for a cosmology with $h=0.5$ and $\Omega_0=1$. The details of the modelling are explained in Section 3.2. The reader is invited to note that the apparent flux in the submm range is almost insensitive to redshift, because the shift of the 100-μm bump counterbalances the distance dimming.

various authors (see especially White & Rees 1978, Schaeffer & Silk 1985, Evrard 1989, Cole 1991 and Blanchard, Valls-Gabaud & Mamon 1992). The modelling of these processes, complemented by star formation, stellar evolution and stellar feedback to the interstellar medium (ISM), has been achieved at various levels of complexity, in the so-called *semi-analytic* approach, which has been successfully applied to the prediction of the statistical properties of galaxies (Lacey & Silk 1991; White & Frenk 1991; Kauffmann, White & Guiderdoni 1993; Lacey et al. 1993; Cole et al. 1994; Kauffmann, Guiderdoni & White 1994; Heyl et al. 1995; Kauffmann 1995, 1996; Baugh, Cole & Frenk 1996a,b; Baugh et al. 1998). It turns out that, in spite of differences in the details of the models, these studies lead to conclusions in the UV, visible and (stellar) NIR which are remarkably similar.

None of these models has been applied so far to the prediction of the properties of galaxies in the IR and submm ranges. This is the main aim of this paper, which proposes a simple version of the semi-analytic approach and gives predictions of faint counts at wavelengths between 15 μm and 1.4 mm. This first study also intends to identify some of the difficulties arising in such a modelling. Section 2 quickly reviews the main physical processes which have to be introduced in order to describe the formation of galaxies: the non-dissipative collapse of perturbations, the dissipative collapse of the gas, star formation and evolution, and feedback. Section 3 addresses the peculiar issue of dust absorption and re-emission in the IR and submm. Section 4 extracts useful information from the recent UV/visible deep surveys, and uses the new constraint arising from the CIB in order to generate a family of evolutionary scenarios. Section 5 gives the IR/submm counts predicted from these scenarios. Finally, Section 6 briefly discusses these results,

as well as the shortcomings of such models, and concludes.

In a previous study, we showed that the CIB can be disentangled with a family of evolutionary scenarios which predict steep submm counts, and that the observations with *ISO* (at 175 μm) will soon constrain the IR/submm evolution at $z \sim 1$ and beyond (Guiderdoni et al. 1997). Here we present the details of the modelling and apply it to other observations, more specifically in SCUBA bands (through the narrow submm atmospheric windows). A preliminary version of this work was presented in Guiderdoni et al. (1996). A forthcoming paper (Hivon et al. 1998, in preparation) will show simulations of the anisotropies of the diffuse submm background due to galaxies, and will study the possibility of their detection with current and forthcoming instruments. Other papers in this series will try to overcome some of the shortcomings of this first study.

2 A SCHEMATIC VIEW OF GALAXY FORMATION

2.1 Non-dissipative collapse

The formation and evolution of a galaxy in its dark matter halo can be briefly sketched as follows. The initial perturbation, which is gravitationally dominated by non-baryonic dark matter, grows and collapses. After the (non-dissipative) collapse, and subsequent violent relaxation, the halo virializes, through the formation of a mean potential well seen by all particles, which consequently share the same velocity distribution. As detailed in the Appendix A, we use the classical top-hat model for spherically symmetric perturbations, and we compute the mass distribution of collapsed haloes from the peaks formalism (Bardeen et al. 1986), as in Lacey & Silk (1991) and Lacey et al. (1993). Hereafter, we shall consider the SCDM model with $H_0 = 50$ km s^{-1} Mpc^{-1}, $\Omega_0 = 1$, $\Lambda = 0$, and $\sigma_8 = 0.67$ as an illustrative case. We take a baryonic fraction $\Omega_{\rm bar} = 0.05$, consistent with primordial nucleosynthesis. The redshift evolution of the number density and formation rate of collapsed haloes is plotted in Fig. 2.

2.2 Cooling and dissipative collapse

The baryonic gas cools in the potential wells of dark matter haloes, by a process identical to cooling flows observed at the centre of rich clusters. The cooling time at halo radius r is

$$t_{\rm cool}(r) = \frac{3}{2}\frac{n_{\rm tot}(r) k T_{\rm V}}{n_{\rm e}^2(r)\Lambda(T_{\rm V})} = 3\pi G \mu_{\rm e}^2 m_{\rm p}^2 \frac{\Omega_0}{\Omega_{\rm bar}}\frac{r^2}{\Lambda(T_{\rm V})}, \quad (1)$$

with $\mu_{\rm e} = 1.14$ for ionized primordial gas. The cooling curve $\Lambda(T)$ takes into account various cooling processes. We do not consider the metallicity dependence of $\Lambda(T)$. Neglecting this dependence leads to an *overestimate* of cooling times, which are already very short. The equation $t_{\rm cool}(r_{\rm cool}) = t(z)$ defines a cooling radius $r_{\rm cool}$ as a function of redshift z. At this redshift, only gas inside $r_{\rm cool}$ (or the virial radius $r_{\rm V}$ if $r_{\rm cool} > t_{\rm V}$) cools and is available for star formation. This cooling criterion introduces a high-mass cut-off in the mass distribution of cold baryonic cores. At the low-mass end, the cooling is so efficient that almost all the gas can cool, leading to a slope of the mass distribution of baryonic cores $n(M_{\rm bar})\mathrm{d}M_{\rm bar} \propto M_{\rm bar}^{-1.95}\mathrm{d}M_{\rm bar}$ at redshift $z = 0$, which is close to the slope $N(M)\mathrm{d}M \propto M^{-2}\mathrm{d}M$ for the number density of collapsed haloes. This is the so-called 'overcooling' problem (Cole 1991; Blanchard et al. 1992).

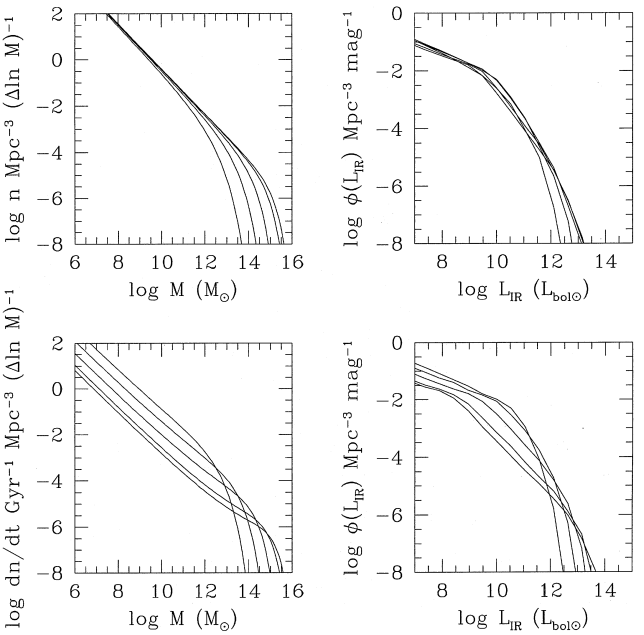

Figure 2. Number density and formation rate of collapsed haloes, and their relation to two modes of star formation. The left-hand panels show the number density of collapsed haloes (top) and the formation rate of collapsed haloes (bottom) computed for the SCDM model with $h = 0.5$, $\Omega_0 = 1$ and $\sigma_8 = 0.67$. The curves are plotted for redshifts $z = 3.67$, 1.99, 0.92, 0.23 and 0 (for increasing number densities at the high-mass end). The right-hand top panel shows the evolution of the IR luminosity function at the same redshifts, in the so-called 'quiescent' mode of star formation with $\beta = 100$, $\alpha = 5$ and $V_{\rm hot} = 130$ km s^{-1}. The increase of the number of galaxies at all masses, as time goes on, is similar to the increase of the number of haloes, and reflects the accumulation of galaxies. The right-hand bottom panel shows the evolution of the IR luminosity function at the same redshifts, in the so-called 'burst' mode of star formation with $\beta = 10$. The galaxies undergo strong starbursts which act as beacons at the epochs of their initial collapses. Consequently, the evolution of the luminosity function reflects the formation rate of new haloes, with the characteristic crossing of the luminosity functions between low and high masses.

The final radius of the cold gas in rotational equilibrium is related to the initial radius by conservation of angular momentum (Fall & Efstathiou 1980). Approximately, $r_{\rm D} \sim \lambda \min(r_{\rm V}, r_{\rm cool})$, with the dimensionless spin parameter $\lambda \equiv J|E|^{1/2}G^{-1}M^{-5/2} \simeq 0.05 \pm 0.03$ (Barnes & Efstathiou 1987; Efstathiou et al. 1998; Zurek, Quinn & Salmon 1988). Previous studies used only the mean value of λ in this formula. Hereafter, we introduce the λ distribution from Barnes & Efstathiou (1987) model C0–4 (their fig. 11). According to a fit based on fig. 3 of Fall & Efstathiou (1980), the exponential disc which forms from the dissipative collapse of the gas has a length-scale $r_0 \simeq 1.26\lambda^{1.17}\min(r_{\rm V}, r_{\rm cool})$ and a radius including half the cold baryonic mass $r_{1/2}/r_0 = 1.68$. A dynamical time-scale in the disc-like core is $t_{\rm dyn} \equiv 2\pi r_{1/2}/V_{\rm c}$. It is important to note that only discs can form in this formalism. The formation of elliptical galaxies

(and of bulges of spiral galaxies) has to be explained by the merging of discs. Kauffmann et al. (1993) and Cole et al. (1994) showed that this merging process can easily explain the current fraction of gEs among bright galaxies.

2.3 Star formation

Locally, the SFR depends on numerous physical parameters. Nevertheless, phenomenological studies seem to show that, on galaxy scales, the SFR per unit surface density is proportional to the total gas surface density (neutral plus molecular) divided by the dynamical time-scale of the disc (Kennicutt 1989, 1998). So we shall hereafter assume that the star formation time-scale, t_*, is proportional to the dynamical time-scale of the disc, $t_{\rm dyn}$, and we introduce a first efficiency factor β. With $t_* \equiv \beta t_{\rm dyn}$, we take

$$SFR(t) = \frac{M_{\rm gas}(t)}{t_*}. \qquad (2)$$

Fig. 3 shows the predicted t_* histogram compared to the histogram of 'Roberts times' for a sample of 63 bright disc galaxies observed by Kennicutt, Tamblyn & Congdon (1994). The Roberts time is defined as $t_{\rm R} \equiv (M_{\rm H\,I} + M_{\rm H_2})/SFR(t_0)$, where $M_{\rm H\,I}$ is the gas mass in the H I phase measured from the 21-cm line, $M_{\rm H_2}$ is the gas mass in the H_2 phase measured from the CO line, and $SFR(t_0)$ is the total star formation rate measured from the Hα line, under an assumption about the shape of the initial mass function (hereafter this is Salpeter IMF). The interesting result is that the model correctly predicts the *shape* and *width* of the histogram. We emphasize that this agreement is due to both the range of halo densities [scaling as $(1+z_{\rm coll})^3$] *and* dimensionless spin parameters λ. Without the λ scatter, the predicted distribution would be about three times too narrow. The average value of the observed histogram can be reproduced by taking $\beta \simeq 100$ for our SCDM model.

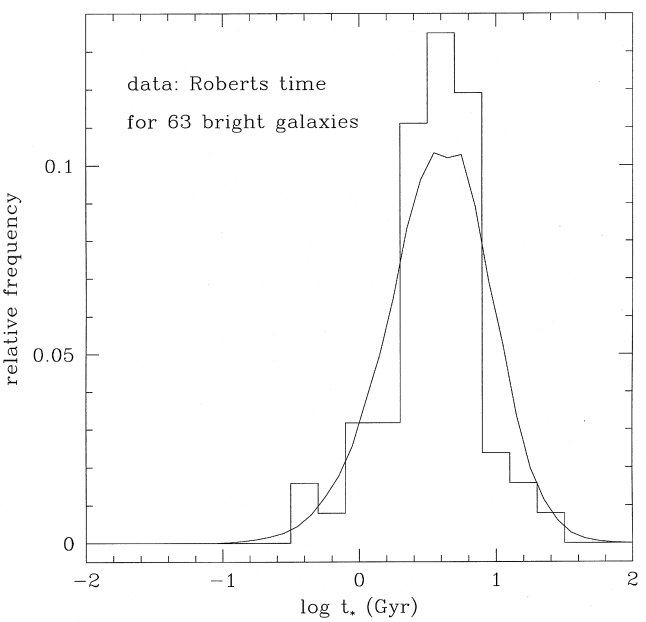

Figure 3. Distribution of the charactierstic SFR time-scales for the 'quiescent' mode of star formation ($\beta = 100$, $V_{\rm hot} = 130$ km s^{-1} and $\alpha = 5$). Only galaxies with $V_{\rm c} > V_{\rm hot}$ are retained. The histogram shows the data for a sample of 63 bright disc galaxies analysed by Kennicutt et al. (1994).

Finally, for sake of simplicity, we use a Salpeter IMF with index $x = 1.35$. Stars have masses $0.1 \leq m \leq 120$ M$_\odot$. We also assume that the mass fraction blocked in dark objects with masses below 0.1 M$_\odot$ is negligible.

2.4 Stellar feedback

The explosion of massive stars can expel gas from the galaxies and quench star formation, leading to a strong increase of the mass-to-luminosity ratios in small objects. Observationally, H I holes and X-ray superbubbles are good evidence that such galactic winds are present in galaxies. The stellar feedback is introduced in a similar way by most authors, following the original work by Dekel & Silk (1986). By equating the gas binding energy to the thermal energy ejected by supernovae, one gets

$$\frac{1}{2} M_{\rm gas}(t) \left(\frac{V_{\rm esc}}{V_{\rm c}}\right)^2 V_{\rm c}^2 = \epsilon \int_0^{t_{\rm W}} \tau_*(t') \eta_{\rm SN} E_{\rm SN} {\rm d}t', \qquad (3)$$

where $\eta_{\rm SN}$ is the number of SNe per unit mass of stars, depending on the IMF. For our choice of IMF, $\eta_{\rm SN} = 7.4 \times 10^{-3}$ M$_\odot^{-1}$. The output mechanical energy of a SN is $E_{\rm SN} \sim 10^{51}$ erg. The escape velocity at radius $r \leq r_{\rm V}$ in a singular isothermal sphere truncated at radius $r_{\rm V}$ is $V_{\rm esc}(r) = \sqrt{2} V_{\rm c} [1 - \ln(r/r_{\rm V})]^{1/2}$. The maximum of the λ distribution corresponds to $r_{1/2}/r_{\rm V} \simeq 0.05$, leading to $V_{\rm esc}/V_{\rm c} \simeq 2.8$. Since much of this energy is subsequently radiated away, we insert a second efficiency factor $0 \leq \epsilon \leq 1$. After some algebra, the mass fraction of stars F_* forming before the triggering of the galactic wind at time $t_{\rm W}$ is given by

$$F_* \equiv \frac{M_*(t_{\rm W})}{M_*(t_{\rm W}) + M_{\rm gas}(t_{\rm W})} = [1 + (V_{\rm hot}/V_{\rm c})^\alpha]^{-1}, \qquad (4)$$

with $\alpha = 2$ and $V_{\rm hot} \equiv (V_{\rm c}/V_{\rm esc})(2\eta_{\rm SN} E_{\rm SN})^{1/2} \epsilon^{1/2} = 310\ \epsilon^{1/2}$ km s^{-1} for the Salpeter IMF. Nevertheless, there is much uncertainty on these parameters because of the cooling of supernova remnants before wind triggering. For instance, numerical simulations seem to suggest that $\epsilon \sim 0.1$ (Thornton et al. 1998). Cole et al. (1994) introduced a fit based on smoothed particle hydrodynamics (SPH) simulations of galaxy formation in which most of the feedback effect is due to momentum exchange rather than to ISM heating (Navarro & White 1993). For a typical feedback parameter $f_{\rm V} = 0.1$, the numerical simulations can be fitted with $\alpha = 5$ and $V_{\rm hot} = 130$ km s^{-1}. We shall hereafter take these values as our standard parameters. The situation is still complicated by the existence of *non-local* feedback processes in addition to the local ones. Blanchard et al. (1992) and Efstathiou (1992) suggest that high-z re-ionization of the IGM could prevent cooling in haloes with circular velocities below $V_{\rm equ} \sim 20$ to 50 km s^{-1}, and possibly as high as $\sim (200)^{1/3} V_{\rm equ}$ in case of adiabatic collapse. So it is very likely that the overall quenching of dwarf formation depends on redshift. Introducing this redshift dependence of dwarf formation partly alleviates the problem of the steep slope of the luminosity function (see, e.g., Kauffmann et al. 1993). So the situation appears to be very complicated, in the

absence of a global theory of feedback processes. In the following, we shall simply model the combination of local and non-local feedbacks by introducing a simple $(1+z_{\rm coll})$ dependence for $V_{\rm hot}$.

2.5 Spectral evolution of the stellar population

A model of spectrophotometric evolution is used to compute the age dependence of the gas content, the UV to NIR spectra of the stellar populations, and the mass-to-luminosity ratios. The stars are placed on the zero-age main sequence of the HR diagram according to the IMF. The model uses compilations of stellar evolutionary tracks, taking into account the various stages of stellar evolution in order to compute at each time-step the distribution of stellar populations in the HR diagram. This distribution is combined with a library of stellar spectra and gives the synthetic spectrum $F_{*\lambda}$. At the end of their lifetimes, stars die and return a fraction of their mass to the ISM. The model which is used here is described in Guiderdoni & Rocca-Volmerange (1987, 1988) and Rocca-Volmerange & Guiderdoni (1988), and includes upgraded stellar tracks from Schaller et al. (1992) and Charbonnel et al. (1996).

Panel (a) of Fig. 4 shows the grid of models with various t_* from 0.33 to 20 Gyr, which are introduced in order to follow the relative gas content of the galaxy $g(t)\equiv M_{\rm gas}(t)/M_{\rm bar}$. The heavy elements synthesized by stars are injected into the ISM. The metallicity of the gas is estimated from the instant recycling approximation $Z_{\rm g}(t)=-y_z\ln g(t)$ with a yield y_z depending on the choice of the IMF. Panel (b) shows the time variation of $Z_{\rm g}(t)$ for the grid of models. The photometric properties can be computed after taking into account the intrinsic extinction (see the following section). As an example, panel (c) gives the face-on $B-V$ colours.

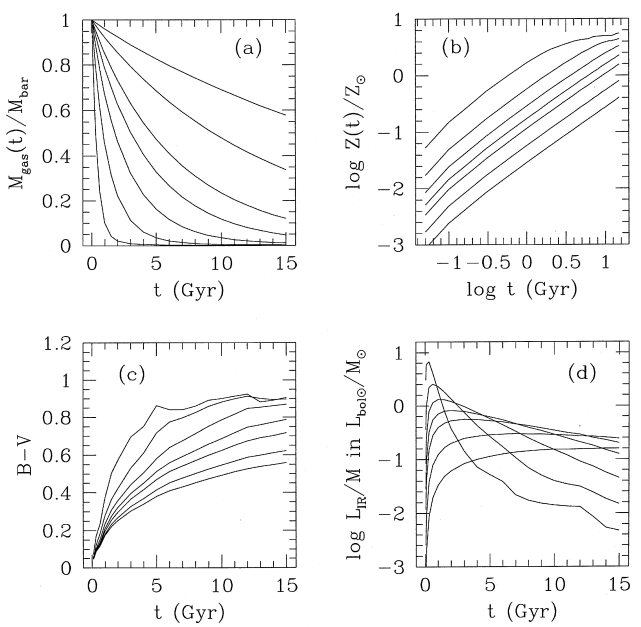

Figure 4. Evolution of various quantities for a grid of models with $t_*=0.33$, 1, 2, 3, 5, 10 and 20 Gyr. (a) Gas fraction (from bottom to top). (b) Gas metallicity (from top to bottom). (c) $B-V$ colour (from top to bottom, taking into account face-on internal extinction). (d) Luminosity re-emitted by dust in the IR/submm (from top to bottom at 1 Gyr).

2.6 The slope of the luminosity function

Before examining the modelling of the IR emission of galaxies, we would like to comment briefly on the slopes of the *B*-band luminosity and gas mass functions obtained by this simple version of the semi-analytic approach.

In spite of the variety of SFR histories, and of the strong variation of the mass-to-luminosity ratios on time-scales of a few Gyr, the *shape* of the luminosity function in the absence of feedback processes is surprisingly similar to that of the baryonic mass function. For $\phi(L_B){\rm d}L_B\propto L_B^s{\rm d}L_B$, our model with $\beta=100$ and the standard mass loss ($\alpha=5$ and $V_{\rm hot}=130$ km s^{-1}) gives $s=-1.4$, whereas Loveday et al. (1992) find $s=-1$. Such an uncomfortable situation is a robust result of *all* the recent attempts to model galaxy formation and evolution in a semi-analytic approach (see Cole et al. 1994 and Kauffmann et al. 1994). Although it seems to be in disagreement with the nearby surveys (but other surveys seem to suggest an increase of the slope at the faint end, e.g. Marzke, Huchra & Geller 1994), this steep slope is necessary to reproduce the deep redshift surveys (down to $B_{\rm J}<24$) and the faint galaxy counts (down to $B_{\rm J}<28$). Subtle selection effects due to surface brightness could explain the discrepancy between the nearby luminosity function and the high-z one (McGaugh 1994; Lobo & Guiderdoni 1998, in preparation).

Indeed, this type of selection effect can be suspected because the predicted gas mass function is in better agreement with the observational data. The predicted mass distribution of gas at redshift $z=0$ has a slope $n(M_{\rm gas}){\rm d}M_{\rm gas}\propto M_{\rm gas}^{-1.3}{\rm d}M_{\rm gas}$ (with the standard values or the parameters). Smaller objects form earlier on an average, with higher densities, smaller $t_{\rm dyn}$ and smaller t_*, and, consequently, they are more affected by mass-loss and their relative gas content is lower. It is possible to correct statistically the total gas mass function in order to predict an H I mass function and compare it to the observational slope -1.35 determined by Briggs & Rao (1993). In the sample of 63 disc galaxies gathered by Kennicutt et al. (1994), there is no systematic trend for $M_{\rm H\,I}/M_{\rm gas}$ versus $M_{\rm gas}$, $t_{\rm R}$, or the SFR. We have made a histogram of $\log(M_{\rm H\,I}/M_{\rm gas})$, with values from -1 to 0, and we have distributed the predicted number density at $M_{\rm gas}$ into the range of $M_{\rm H\,I}$ values according to this histogram. The effect of this correction turns out to be rather small. Thus there is a good agreement of the predictions with the observations. It is worthwhile to emphasize that the slope -1.35 of the data depends on the volume corrections of the survey for low-mass objects, and is somewhat uncertain.

3 SPECTRAL EVOLUTION OF DUST EMISSION

3.1 Dust absorption

Part of the energy released by stars is absorbed by dust and re-emitted in the IR and submm ranges. The derivation of the IR/submm spectrum is a three-step process: (i) computation of the optical thickness of the discs, (ii) computation

of the amount of bolometric energy absorbed by dust, and (iii) computation of the spectral energy distribution of dust emission. The modelling of these steps is not an easy task, since it requires addressing confused issues such as the chemical evolution of the dust, and the geometrical distribution of dust relatively to stars.

We assume that the gas is distributed in an exponential disc with truncation radius r_g and mean hydrogen column density $\langle N_H(t)\rangle = M_{gas}(t)/1.4 m_H \pi r_g^2$. The factor 1.4 accounts for the presence of helium. If r_{25} is the isophotal radius at 25 mag arcsec^{-2}, the observations give $r_g/r_{25} \simeq 1.6$ (Bosma 1981). The r_{25} radii are consistently computed from the B magnitudes and r_0 radii of the galaxies. Fig. 5 shows the mean total and gas surface densities inside r_g at redshift $z=0$. These surface densities fairly correspond to the crude estimate $\langle N_H(t)\rangle = 6.8\times10^{21} g(t)$ atom cm^{-2} used in Guiderdoni & Rocca-Volmerange (1987) and Franceschini et al. (1991, 1994). As noted by Guiderdoni & Rocca-Volmerange (1987), a galaxy with $g \simeq 0.20$ has an hydrogen column density $\langle N_H\rangle \simeq 1.4\times10^{21}$ atom cm^{-2}, in good agreement with the observational value for late-type discs, in spite of the uncertainties in this estimate (Guiderdoni 1987).

The mean optical thickness inside r_g is given by

$$\tau_\lambda(t) = \frac{1}{1.086}\frac{A_\lambda}{A_V}[Z_g(t)]\frac{A_V}{E_{B-V}}\frac{E_{B-V}}{N_H}[Z_g(t)]\langle N_H(t)\rangle \qquad (5)$$

$$= \left(\frac{A_\lambda}{A_V}\right)_{Z_\odot}\left[\frac{Z_g(t)}{Z_\odot}\right]^s\left(\frac{\langle N_H(t)\rangle}{2.1\times10^{21}\ \text{atom cm}^{-2}}\right). \qquad (6)$$

As in Guiderdoni & Rocca-Volmerange (1987) and Franceschini et al. (1991, 1994), the extinction curve depends on the gas metallicity $Z_g(t)$ according to power-law interpolations based on the solar neighbourhood and the Magellanic Clouds, with $s=1.35$ for $\lambda < 2000$ Å and $s=1.6$ for $\lambda > 2000$ Å. The extinction curve for solar metallicity is taken from Mathis, Mezger & Panagia (1983).

It is not clear whether the discs of 'normal' spirals are optically thin or optically thick. Catalogues of galaxies (such as the classical RC2 and the RSA) suggest $\tau_B = 0.7$ for spirals. On the other hand, several studies have pointed out the possibility of optically thick discs (see, e.g., Disney, Davies & Philipps 1989, and references therein). Since the gas decrease is counterbalanced by the metallicity increase, the optical thickness of our grid of models is maximal for $g(t) = e^{-s} \simeq 0.20$ with $s=1.6$. Late-type discs spend most of their lifetime at optical depths $\tau_B \simeq 0.4$–0.7, in good agreement with what is suggested in the RC2 or RSA, and with the estimates of Rowan-Robinson (1992) based on *IRAS* results. Fig. 6 gives the predicted distribution of optical thicknesses, which fairly compares with a sample of normal spirals and luminous IR galaxies (Franceschini & Andreani 1995).

As in Guiderdoni & Rocca-Volmerange (1987) and Franceschini et al. (1991, 1994), we also assume a simple geometric distribution where the gas and the stars which contribute mainly to dust heating are distributed with equal height-scales in the discs. If $\tau_\lambda(t)$ is the optical thickness of the discs at wavelength λ and time t, the extinction correction (averaged over inclination angle i) is

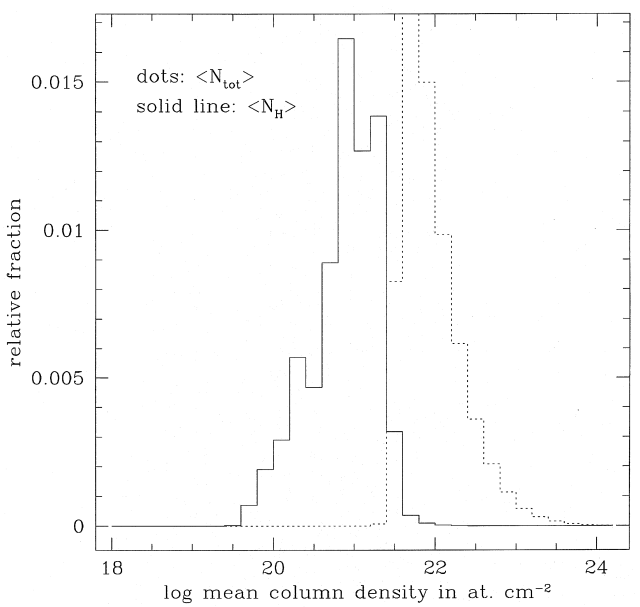

Figure 5. Distribution of mean column densities at $z=0$, in atom cm^{-2}, for galaxies with $SB_e < 25$ mag arcsec^{-2}, and the 'quiescent' mode of star formation ($\beta=100$, $\alpha=5$ and $V_{hot}=130$ km s^{-1}). Dotted line: log $\langle N_{tot}\rangle$; solid line: log $\langle N_H\rangle$.

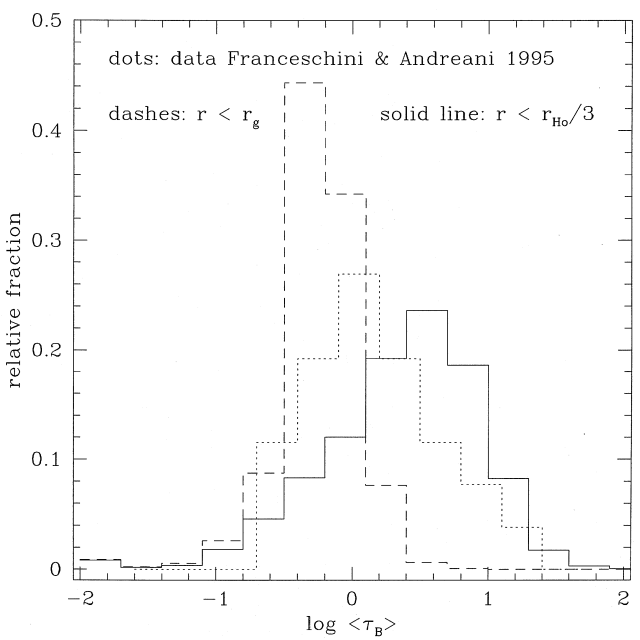

Figure 6. Distribution of mean, face-on optical depth in the B band at $z=0$, for the 'quiescent' mode of star formation ($\beta=100$, $\alpha=5$ and $V_{hot}=130$ km s^{-1}). Two ways of computing τ_B are considered. Dashes: mean optical depth inside the gas radius ($r_g = 1.6 r_{25}$). Solid line: mean optical depth inside one-third of the Holmberg radius (at 26.5 mag arcsec^{-2}). The dotted line shows the observational distribution in a sample of normal spirals and luminous IR galaxies from Franceschini & Andreani (1995). The total dust quantity derived from 1.3-mm observations is distributed within one-third of the Holmberg radius, and an observational estimate of τ_B is computed. The observational distribution peaks at the value $\langle\tau_B\rangle \sim 1$, and is bracketed by the two predicted histograms.

$$A_\lambda(t) = -2.5 \log \left\langle \frac{1-\exp[-a_\lambda \tau_\lambda(t)/\cos\, i]}{a_\lambda \tau_\lambda(t)/\cos\, i} \right\rangle_i, \quad (7)$$

providing that the stars and gas have the same height-scales. The factor $a_\lambda \equiv (1-\omega_\lambda)^{1/2}$ crudely takes into account the effect of the albedo ω_λ (from Draine & Lee 1984) for isotropic scattering (Natta & Panagia 1984) and relates extinction to absorption. This 'slab' geometry is intermediate between the 'screen' geometry $\exp(-a_\lambda \tau_\lambda/\cos\, i)$ and the 'sandwich' geometry (with zero height-scale for dust) $[1+\exp(-a_\lambda \tau_\lambda/\cos\, i)]/2$ which respectively lead to larger and smaller absorption. Observational analyses seem to suggest that this 'slab' geometry is the best guess to fit the data (see, e.g., Franceschini & Andreani 1995; Andreani & Franceschini 1996).

Finally, the bolometric luminosity which is absorbed by dust and released in the IR/submm is

$$L_{\rm IR}(t) = \int F_{*\lambda}(t)[1-10^{-0.4A_\lambda(t)}]{\rm d}\lambda. \quad (8)$$

Panels (c) and (d) of Fig. 4 respectively show the face-on extinguished $B-V$ colours and the IR bolometric luminosities per unit mass of galaxy for a grid of models with various t_*. The corresponding range of IR-to-blue luminosity ratios $0.06 \leq L_{\rm IR}/\lambda_B L_B \leq 4$ is very similar to the observed range for optically selected samples; for instance, the sample drawn from the Zwicky Catalogue with $m_z < 15.7$ mag in Soifer et al. (1987), and characterizes 'mild starbursts' and LIGs. The IR-to-blue luminosity ratios are sensitive to τ_B and the geometry. If there are tidally induced gas inflows resulting in smaller r_g and a 'screen'-like gas distribution, this ratio can easily reach 10–100 as in the ULIGs. We hereafter keep the LIG-type efficiency of conversion between the optical and the IR as a conservative estimate, and we shall consider the population of ULIGs in Section 4.3

3.2 Dust emission

The emission spectra of galaxies are computed as a sum of various components, according to the method developed by Maffei (1994), which uses the observational correlations of the *IRAS* flux ratios 12 μm/60 μm, 25 μm/60 μm and 100 μm/60 μm with $L_{\rm IR}$ (Soifer & Neugebauer 1991). These correlations are extended to low $L_{\rm IR}$ with the samples of Smith et al. (1987) and especially Rice et al. (1988).

Several components are considered in the model spectra.

(1) Polycyclic aromatic hydrocarbons (PAH). Because of their small size (≤ 1 nm), these molecules never reach thermal equilibrium when they are excited in a UV/visible radiation field. Their temperature fluctuates and can reach a value much higher than the equilibrium temperature, explaining the 12-μm excess and the bands at 3.3, 6.2, 7.7, 8.6 and 11.3 μm. Their template emission spectrum is taken from the model by Désert, Boulanger & Puget (1990).

(2) Very small grains (VSG). They are made of graphite and silicates. These dust grains have sizes between 1 and 10 nm. As the PAH, they never reach thermal equilibrium. Consequently, their emission spectrum is much broader than a modified blackbody spectrum at a single equilibrium temperature. The template emission spectrum is also taken from the model by Désert et al. (1990).

(3) Big grains (BG). They are also made of graphite and silicates. These dust grains have sizes between 10 nm and 0.1 μm. They (almost) reach thermal equilibrium, and can be reasonably described by a modified black body $\epsilon_\nu B_\nu(T_{\rm BG})$ and emissivity $\epsilon_\nu \propto \nu^m$ with $1 \leq m \leq 2$.

(4) Synchrotron radiation. This non-thermal emission is strongly correlated with stellar activity and, as a consequence, with IR luminosity (see, e.g. Helou, Soifer & Rowan-Robinson 1985). According to observations at 1.4 GHz, this correlation is $L_\nu(1.4\ {\rm GHz}) = L_{\rm IR}/(3.75\times10^{12}\times10^q)$. Here $L_{\rm IR}$ is in W, $\nu_{80} = 3.75\times10^{12}$ Hz is the frequency at 80 μm, and $q \simeq 2.16$ is determined from observations. Then we assume that we can extrapolate from 21 cm down to $\sim$1 mm with a single average slope 0.7, so that $L_\nu = L_\nu(1.4\ {\rm GHz})(\nu/1.4\ {\rm GHz})^{-0.7}$.

The 60/100 colour gives the temperature $T_{\rm BG}$ of the BG, provided that an emissivity index m has been chosen. We hereafter test $m=1$, 1.5 (standard value) and 2. Then the amounts of BG, VSG and PAH are calculated iteratively from the 12/100, 25/100 and 60/100 ratios. The resulting spectra are computed from a few μm to several mm and evolve with $L_{\rm IR}$ such that more luminous galaxies preferentially emit at shorter wavelengths. By construction, these spectra fit the *IRAS* colour correlations. Fig. 7 shows examples of these model spectra for various $L_{\rm IR}$ and three values of the emissivity index for BG.

In spite of its shortcomings, this method takes into account the observed spectral evolution in the IR and submm/mm ranges, while previous works generally use a single template spectrum in the whole spectral range. It is also possible to reproduce the FIR photometry of various individual galaxies by this method (Maffei 1994). Fig. 8

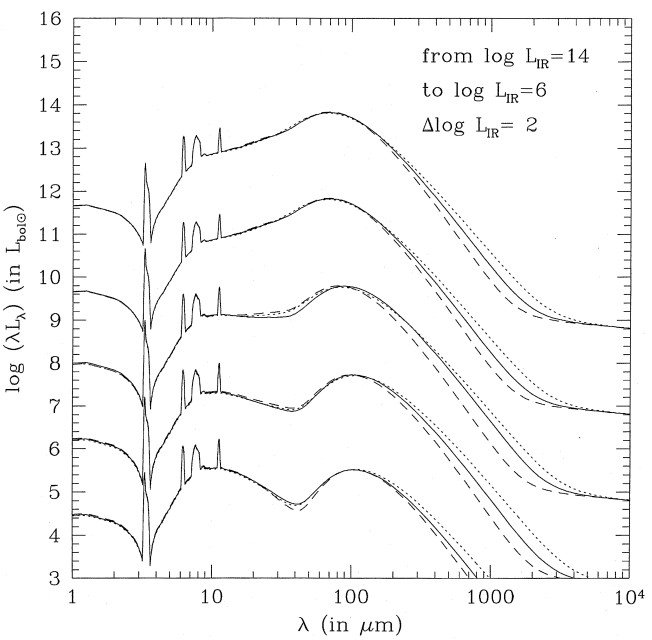

Figure 7. Model spectra in the IR and submm, for IR luminosities 10^6, 10^8, 10^{10}, 10^{12} and 10^{14} $L_{\rm bol\odot}$. Emissivity index of big grains: $m=2$ (dashes), $m=1.5$ (solid lines), $m=1$ (dotted lines).

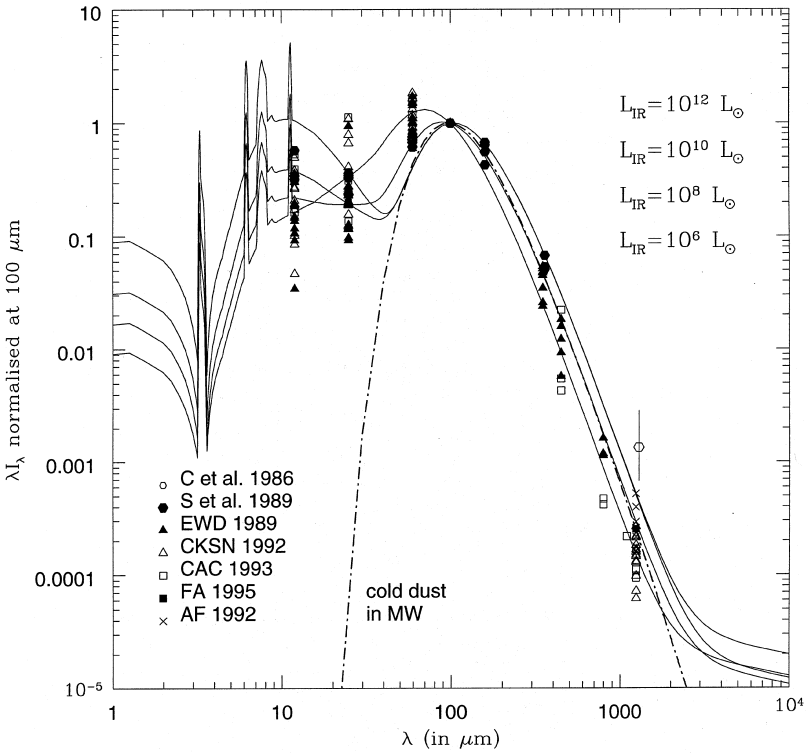

Figure 8. Model spectra with $m=1.5$ superimposed to a compilation of data in the FIR and submm: Chini et al. 1986 (mean value), Stark et al. 1989, Eales et al. 1989, Carico et al. 1992, Andreani & Franceschini 1992, Clements et al. 1993, Franceschini & Andreani 1995 (mean value). The dot-dashed line is a typical spectrum of cold dust in the Milky Way (Reach et al. 1995). Models and data are normalized at 100 μm.

shows a compilation of data superimposed to a series of model spectra. The compiled samples gather galaxies which have been observed at least at one wavelength in the submm range (say, between 200 μm and 1.3 mm) with a positive detection. The various samples are very heterogeneous. They have been obtained with different telescopes and instruments, and focus upon different types of galaxies ('normal' spirals, LIGs, ULIGs). None of them is complete. Moreover, there is very little overlap between the samples, and the few galaxies which have been observed by various authors with various instruments generally have discrepant fluxes. These discrepancies can originate from the choices of beam size and beam chopping. Andreani & Franceschini (1992, 1996) have studied the effect of the finite extension of the submm emission and computed an average aperture correction, which turns out to be rather small.

There is some debate about the presence of very cold dust which could emit at submm wavelengths. Chini et al. (1986), confirmed by Chini & Krügel (1993), claim that the dust seen at *IRAS* wavelengths is unable to reproduce the observed submm emission. On the contrary, Eales et al. (1989), Stark et al. (1989) and Clements et al. (1993) do not detect any evidence for this new component. Chini et al. (1986) interpret their high fluxes as evidence for the existence of cold dust. The value of the derived temperature depends on the choice of the emissivity index of these grains, which can be anything between 1 and 2. Clearly, the uncertainties in the submm emission are large, and the need for a systematic survey of a complete sample is strong. There is no doubt that this will be one of the first targets of SCUBA. Because of these uncertainties, the models with an average index $m=1.5$ plotted in Fig. 8 seem to cover the range of observations at submm wavelengths, except the high fluxes observed by Chini et al. (1986).

4 THE HISTORY OF STAR FORMATION IN THE UNIVERSE

4.1 The 'quiescent' mode of star formation

In this section we will introduce scenarios of evolution which will be used to compute the IR/submm properties of galaxies, and to predict faint galaxy counts and the CIB. The description of these scenarios and their line codes in the figures are summarized in Table 1. While a complete assessment of the energy budget of galaxies would require the monitoring of multiwavelength luminosity functions and galaxy counts (delayed to forthcoming studies), we hereafter wish only to address the issue of the overall evolution of the comoving SFR and gas densities in the Universe. Pei & Fall (1995) and Fall et al. (1996) emphasized the relevance of these quantities to describe the overall evolution of the galaxy population.

Figs 9 and 10 respectively show the predicted SFR and gas evolutions for scenario Q with $\beta=100$. It corresponds to the fit of SFR time-scales in discs, that is, the so-called 'Roberts times' peaking at 3 Gyr and ranging between 0.3 and 30 Gyr (Kennicutt et al. 1994). The feedback parameters are $\alpha=5$ and $V_{\rm hot}=40(1+z_{\rm coll})$ km s^{-1}. This somewhat arbitrary $(1+z)$ dependence is intended to mimic the effect

Table 1. Scenarios of galaxy evolution.

Name	f_{burst} ($\beta = 10$)	f_{quiet} ($\beta = 100$)	% of ULIGs	Line code
Q	0	1	0 %	dots and small dashes
A	$0.04(1+z_{coll})^5$	$1-f_{burst}$	0 %	solid line
B	$0.04(1+z_{coll})^5$	$1-f_{burst}$	5 % at all z_{coll}	dotted line
C	$0.04(1+z_{coll})^5$	$1-f_{burst}$	90 % for $z_{coll} > 3.5$	long dashes
D	$0.04(1+z_{coll})^5$	$1-f_{burst}$	15 % at all z_{coll}	short dashes
E	$0.04(1+z_{coll})^5$	$1-f_{burst}$	$1-\exp -0.02(1+z_{coll})^2$	dots and long dashes

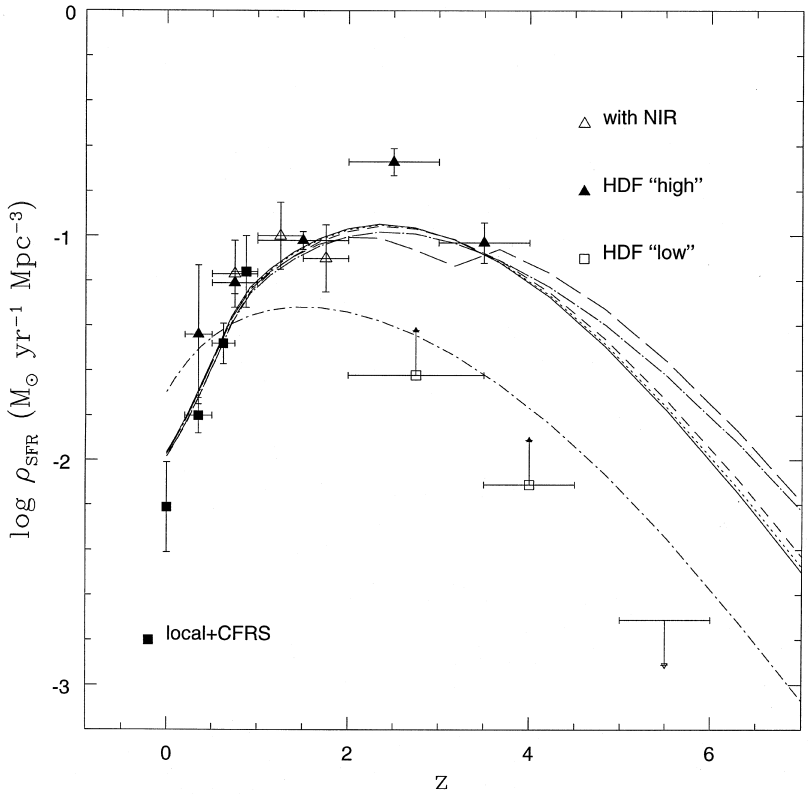

Figure 9. Evolution of the cosmic comoving star formation rate density as computed from rest-frame UV luminosity densities, by using Salpeter IMF with slope 1.35. The UV densities are based on the integration of the luminosity function fit on all magnitudes. The UV fluxes have *not* been corrected for intrinsic extinction. The solid squares are derived from the rest-frame 2800-Å luminosity density in the Canada–France Redshift Survey, and the local value is from the *B*-band luminosity function and average UV − *B* colour (Lilly et al. 1996). The open triangles take into account NIR data to compute photometric redshifts in the Hubble Deep Field (Connolly et al. 1997). The solid triangles come from another photometric-redshift analysis of the HDF (Sawicki et al. 1997), while the open squares with the arrows are lower and upper values from the HDF with redshifts derived from Lyman-continuum drop-outs (Madau et al. 1996). Scenario Q ('quiescent' mode, $\beta = 100$) is plotted with dots and small dashes. It is unable to reproduce the steep decline of ρ_{SFR} between redshifts 1 and 0. Other scenarios involve an increasing fraction of the 'burst' mode ($\beta = 10$) with redshift, producing a population of LIGs. Scenario A (solid line) has no ULIGs. Various quantities of ULIGs are included in scenarios B (dotted line), C (long dashes), D (short dashes) and E (dots and long dashes). See Table 1 for details and summary of lines codes. The SFRs slightly differ because t_* is considered as an exponential time-scale for the LIGs and a burst duration for the ULIGs.

of global reheating at high redshift and avoids a stepwise change of V_{hot} at $z = 2$ caused by a bimodal regime. This has almost no effect at low *z*, but it changes the high-redshift behaviour of the SFR density.

Clearly, the SFR density in scenario Q does not decline fast enough between $z = 1$ and the local Universe, and, correspondingly, gas is not consumed sufficiently. The impossibility to reproduce the peak of SFR density with star formation histories similar to those in discs is not surprising. We know that their present SFR time-scales (the Roberts times) are large, and that their SFRs have not changed significantly during the last few billion years (Kennicutt et al. 1994).

The prediction for the evolution of the comoving SFR density is very similar to the result given by Baugh et al. (1998), although their model involves a more accurate procedure to compute the merging history of haloes (Cole et al. 1994). As in our model, they choose a SFR proportional to the ratio of the cold gas content to the dynamical time. However, galaxies within haloes can merge after spiralling to the centre of the haloes induced by dynamical friction. During the merging, all the available gas is quickly con-

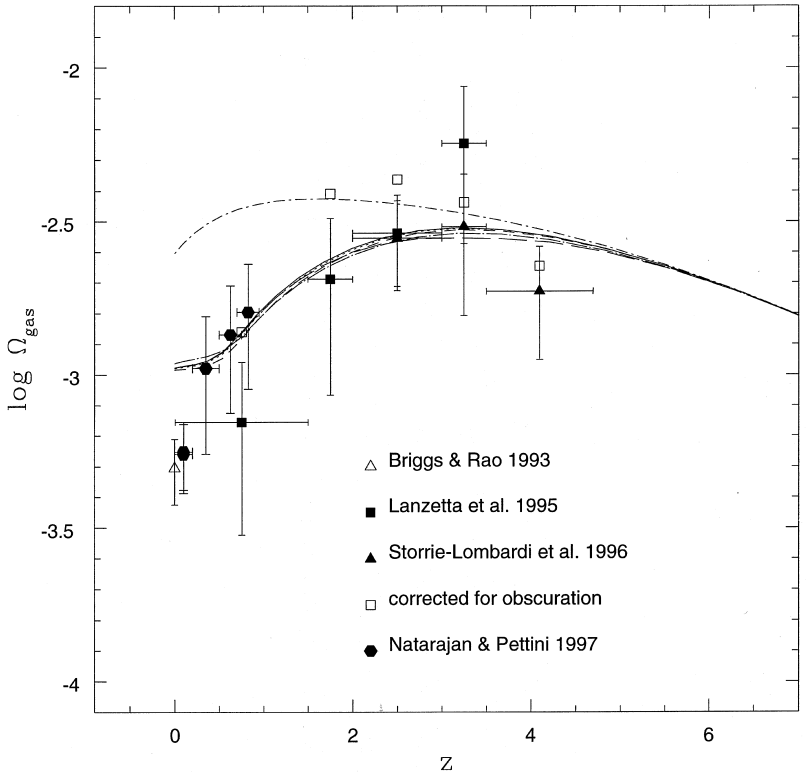

Figure 10. Evolution of the cold gas density parameter in damped Lyman-α absorbers. Solid squares: data without the APM QSO survey (Lanzetta, Wolfe & Turnshek 1995). Solid triangles: data including the APM QSO survey. Open squares: tentative correction for selection effects due to QSO obscuration (Storrie-Lombardi et al. 1996). Solid hexagons: Natarajan & Pettini (1997). Open triangle: local estimate from H I surveys (Briggs & Rao 1993). Line codes of scenarios Q, A, B, C, D and E are given in Table 1. The various scenarios involving the 'burst' mode consume more gas than the 'quiescent' mode (dots and short dashes).

verted into stars. In spite of this explicit implementation of a kind of 'burst' mode, starbursting does not seem to affect significantly the SFR history, and the evolution they predict does not reproduce the steep decline of the SFR density between $z=1$ and 0. Probably the modelling of dynamical friction alone underestimates the true magnitude of the interacting and merging processes between galaxies in merging haloes.

4.2 The 'burst' mode of star formation

We now wish to introduce another mode of star formation with $\beta=10$. The SFR time-scales are now much shorter. As a result, the evolution of the luminosity function differs from the evolution in scenario Q involving the 'quiescent' mode of star formation. As shown in Fig. 2, the luminosity function of the 'quiescent' mode is built up by the accumulation of light coming from all galaxies, and its evolution reproduces the evolution of the mass distribution of collapsed haloes. On the contrary, the luminosity function of the 'burst' mode reproduces the evolution in the formation of haloes. Each generation of halo formation is accompanied by a strong starburst, which acts as a transient beacon. As a consequence, the evolutionary trends of the luminosity functions in the two modes differ strongly.

Since we know that the local Universe is dominated by the 'quiescent' mode, we now consider a mix of two broad types of populations, one with a 'quiescent' star formation rate, the other proceeding in bursts. For the 'burst' mode, we take an involved mass fraction increasing with redshift $f_{\rm burst}(z)=f_{\rm burst}(0)(1+z_{\rm coll})^{\gamma}$, as suggested by the increasing fraction of blue objects showing tidal and merger features at larger z (Abraham et al. 1996). Such a dependence is also consistent with theoretical considerations on the merger rates of galaxy pairs in merged haloes (Carlberg 1990). We limit the scope of the present paper to this phenomenological modelling of $f_{\rm burst}(z)$. This is clearly a point which should be refined in forthcoming studies. Noting that the frequency of galaxy pairs is $\propto(1+z)^{\delta}$, with δ between 2 and 6 at $\pm1\sigma$ (Zepf & Koo 1989; Burkey et al. 1994; Carlberg, Pritchet & Infante 1994), we choose here a high evolution rate $\gamma=5$. Then $f_{\rm burst}(0)$ is set to 0.04 in order to fit the SFR density at low z, resulting in an 'all-burst' behaviour at $z_{\rm coll}\geq0.8$. This will be our scenario A. As appears from Fig. 9, this phenomenological description of the increasing importance of bursts reproduces the steep decline of the SFR density. The origin of this fast evolution has still to be elucidated by a more exhaustive modelling of all interaction processes in the semi-analytic codes which follow the merging history trees of haloes and galaxies. Fig. 9 also shows that the predicted cosmic SFR history has a high-z evolution closer to the one derived from photometric estimates of redshifts rather than that from Lyman-continuum drop-outs. For instance, one should note that at $z=4$, the predicted SFR is 10 times the lower limit derived from the Lyman-continuum drop-outs *without extinction*. As a conse-

quence of the high SFR, the gas content strongly evolves beween $z \sim 2$ and 0, as shown in Fig. 10.

We can now compute the corresponding IR/submm emission by taking the conservative estimate of the average optical thickness and 'slab' geometry as in the 'quiescent' mode. As a result, this population of 'mild starbursts' and 'luminous UV/IR galaxies' (LIGs) have IR-to-blue luminosity ratios in the range $0.06 \leq L_{\rm IR}/\lambda_B L_B \leq 4$ which is characteristic of blue-band-selected samples (Soifer et al. 1987), and should be fitted to the Canada–France Redshift Survey (selected in the observer-frame I_{AB} band, roughly corresponding to the B band at $z \sim 1$), and to high-z HDF galaxies. Galaxies at the peak of the SFR time-scale distribution ($t_* = 0.3$ Gyr) have $L_{\rm IR}/M \simeq 6.3 L_{\rm bol\odot}/{\rm M}_\odot$. Nevertheless, their colours can still be very blue during the burst ($B-V=0.1$ at 0.5 Gyr). The evolution of the comoving luminosity density in various UV/visible bands and at 60 μm is compared to observational estimates in Fig. 11. The local energy budget and its evolution from $z=0$ to 1 seem to be fairly reproduced. The difference between the fits of the comoving SFR and luminosity densities (Figs 9 and 11) originates in the presence of dust absorption. The local UV flux is correctly fitted in Fig. 11, while the local SFR in Fig. 9 is about twice the value deduced from the local UV flux *under the assumption of no extinction.*

By integrating the contribution of sources along the line of sight, we can predict the corresponding diffuse backgrounds. While the results for both scenarios fairly reproduces the COB, as shown in Fig. 12, scenario A does not do much better than scenario Q to reproduce the CIB. Their predictions are clearly barely compatible with the acceptable $\pm 1\sigma$ range recalled in Fig. 13. The mean amplitude of the CIB is twice the prediction, despite our high choice of γ. Consequently, we can strongly suspect the existence of a population of galaxies which are more heavily extinguished.

4.3 A heavily extinguished component

The above-mentioned CIB computed with scenario A seems to be something like a conservative estimate of the minimum IR/submm background due to typical CFRS and HDF galaxies. We now wish to assess how much star formation might be hidden by dust shrouds and introduce an additional population of heavily-extinguished bursts, which are similar to 'ultraluminous IR galaxies', or ULIGs (Clem-

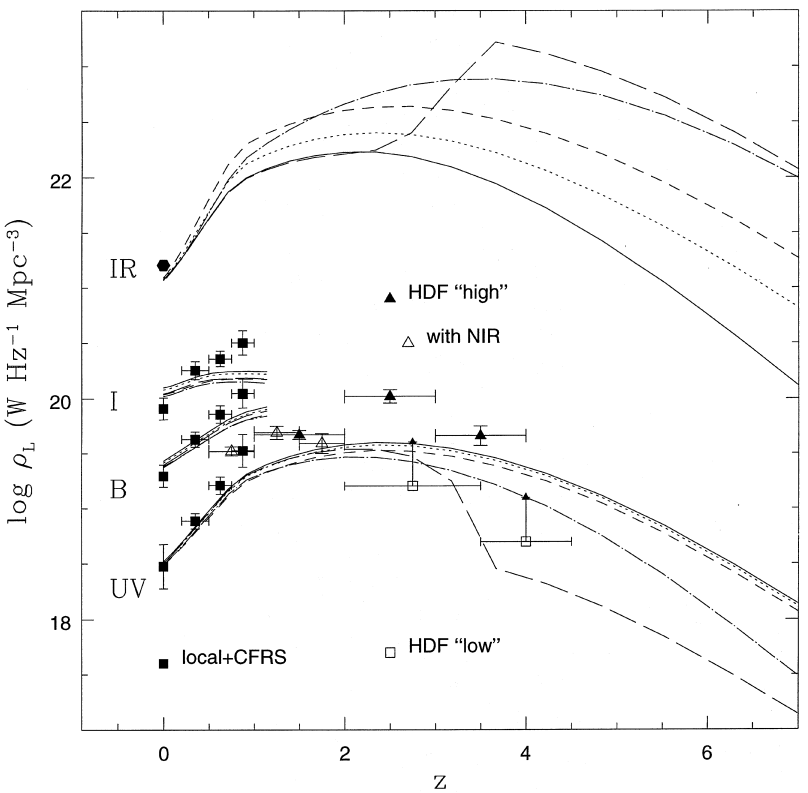

Figure 11. Rest-frame comoving luminosity density. Letters UV, B, I and IR respectively stand for 2800 Å, 4400 Å, 10 000 Å and 60 μm. The emissivity at 1600 Å is about 30 per cent higher than at 2800 Å. The luminosity densities are based on the integration of the luminosity function fit on all magnitudes. Solid squares: local and Canada–France Redshift Survey (Lilly et al. 1996). Open triangles: NIR data are taken into account to compute photometric redshifts in the Hubble Deep Field (Connolly et al. 1997). Solid triangles: other estimates of photometric redshifts in the HDF (Sawicki et al. 1997). Open squares with arrows: HDF with redshifts from Lyman-continuum drop-outs (Madau et al. 1996). Solid hexagon: 60-μm local density corresponding to one-third of the bolometric light radiated in the IR (Saunders et al. 1990). Line codes of scenarios A, B, C, D and E are given in Table 1. The different UV and IR emissions result mainly from different fractions of ULIGs (with a top-heavy IMF and strong extinction), with almost similar SFR histories. Strongly differing high-z IR emission are obtained without being much constrained by the current status of (discrepant) UV/optical observations.

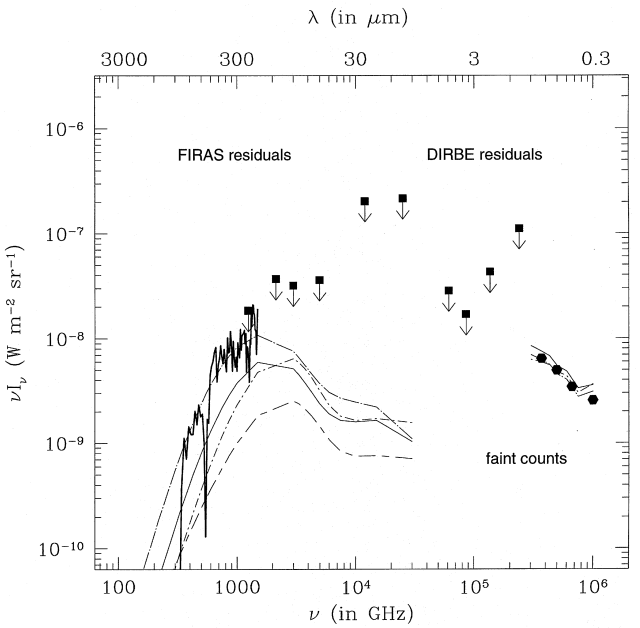

Figure 12. Predictions of the diffuse backgrounds in the FIR/submm and in the optical compared to the current upper limits and detections. The solid squares show the level of *COBE*/DIRBE residuals from Hauser (1995). The similar shapes of the residuals and dark sky suggest that the subtraction of foregrounds has been incomplete and that the plotted values are upper limits. The thick solid line gives the CIB spectrum from the re-analysis of the *COBE*/FIRAS residuals, initiated in Puget et al. (1996) and revisited in Guiderdoni et al. (1997). The solid hexagons show the Cosmic Optical Background (COB) obtained by summing up faint galaxy counts down to the Hubble Deep Field limit. Strictly speaking, this is only a lower limit of the actual COB, but the shallowing of the *U*- and *B*-band counts suggests near-convergence at least at those wavelengths (Williams et al. 1996). The short dashes and long dashes give the prediction for no-evolution integrated up to redshift $z_{\rm for}=8$ in a cosmology with $h=0.5$ and $\Omega_0=1$. The other curves are computed for the SCDM model with $h=0.5$, $\Omega_0=1$, $\sigma_8=0.67$, for scenarios Q, A and E plotted with the line codes of Table 1. Scenarios Q and A are not sufficient to reproduce the CIB. This suggests the existence of an additional population of ULIGs taken into account in scenario E.

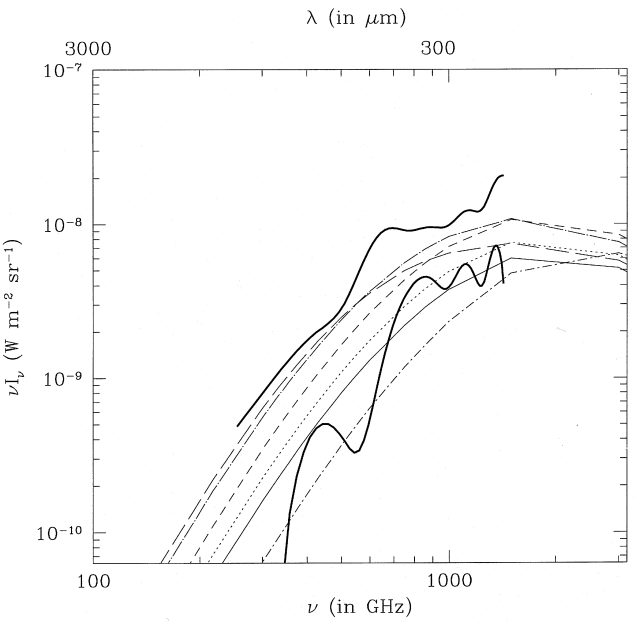

Figure 13. Predictions of the diffuse backgrounds in the FIR/submm (blow up), compared to the acceptable range of the CIB at $\pm1\sigma$ per point (Guiderdoni et al. 1997). Scenarios Q, A, B, C, D and E are plotted with line codes of Table 1. The predictions for the COB are similar to those in Fig. 12.

ents et al. 1996a; Sanders & Mirabel 1996). We maximize their IR luminosity by assuming that all the energy available from stellar nucleosynthesis ($0.007xMc^2$) is radiated in a heavily extinguished medium, yielding a total IR luminosity $L_{\rm IR}/M \simeq 42.5(x/0.40)(t_*/1\ {\rm Gyr})^{-1}L_{\rm bol\odot}/{\rm M}_\odot$, provided that the lifetimes of stars are smaller than the duration t_* of the burst. We take $\langle x\rangle=0.40$ for stars with masses larger than $\sim 5\,{\rm M}_\odot$ (Schaller et al. 1992), and get luminosities which are a factor ~ 20 larger than those of our mild-starburst/LIG mode. As a consequence of this simple model, the starburst radiates only in the IR/submm, and only dark remnants are left when it stops, without the slow evolution of low-mass stars. We distribute this population of ULIGs in two ways. (i) A constant mass fraction of 5 per cent (scenario B) or 15 per cent (scenario D) at all $z_{\rm coll}$, mimicking a scenario of continuous bulge formation as the end-product of interaction and merging. (ii) 90 per cent of all galaxies forming at high $z_{\rm coll}\geq 3.5$ undergo a heavily extinguished burst, mimicking a strong episode of bulge formation. These scenarios are now able to fit both the COB and CIB. Scenarios B and D seem more appropriate to reproducing the CIB at 300 μm, while scenario C, with high-*z* ULIGs, has a strong contribution at larger wavelengths. Of course, these last three cases are only illustrative, and a combination of these solutions would also fit the CIB. For instance, we introduce an ad hoc scenario E with a fraction of ULIGs increasing as $1-\exp[-0.02(1+z_{\rm coll})^2]$. Such a dependence can be obtained if the fraction of ULIGs depends on the mean surface density and optical thickness of discs, which roughly scale as $(1+z_{\rm coll})^2$ in our modelling. As shown by figs. 12 and 13, scenario E nicely reproduces the COB and CIB, and could be considered as our 'best fit'.

It is clear from Fig. 11 that none of the optical data reflects the large differences between these scenarios, although the fraction of light in the IR varies widely at high *z*. In scenario A, the IR/UV ratio decreases with increasing *z* because of the decreasing metallicity of galaxies. In scenarios B and D, this effect is cancelled because the ULIG bursts are assumed to be optically thick, with a top-heavy IMF, and the IR/UV ratio at $z=4$ is similar to that at $z=0$. In scenarios C and E, the IR/UV ratio strongly increases with *z*, and is ~ 100 times higher than for model B at $z=4$. One should note that at this redshift, scenarios C and E are roughly consistent with the lower limits of the UV-luminosity density derived from Lyman-continuum drop-outs, but with 10 times as much SFR as directly derived if extinction is not taken into account. In these scenarios, galaxy formation at high *z* is an almost completely obscured process.

We emphasize that the family of scenarios summarized in Table 1 is introduced within the same SCDM model. The

dissipative and non-dissipative collapses are unchanged, and the characteristic time-scale for the conversion of gas into stars is always proportional to the local dynamical time, which is the most natural time-scale. Given that, we change only the 'fuzzy' astrophysics introduced with the efficiency parameter β. It seems reasonable to *assume* that the efficiency of star formation is typically an order of magnitude greater for interacting galaxies (the 'burst' mode) than for isolated galaxies (the 'quiescent' mode), resulting in a β parameter an order of magnitude lower. While this assumption has yet to be put on firmer grounds, its effect on the global SFR and gas densities is very strong. As a second step, changes in the IMF and extinction can modify the optical and IR/submm energy budget.

5 PREDICTIONS IN THE FIR AND SUBMM

5.1 The FIR luminosity function

Fig. 14 gives predictions for the $z=0$ luminosity function at 60 μm compared with the observational determinations drawn from the *IRAS* Bright Galaxy Sample (Soifer & Neugebauer 1991) and from a compilation of various *IRAS* samples (Saunders et al. 1990). The difference of the two observational luminosity functions at the faint end illustrates the uncertainties. The agreement of the predictions with the data is fair. It is not surprising that scenario Q seems to give a better fit, since most galaxies of the BGS are spirals, mild starbursts and LIGs. All the scenarios involving the burst mode (A to E) give similar results at $z=0$, since the fraction of mass involved in starbursts is low (4 per cent). Burst scenarios with shorter SFR time-scales in the past consumed more gas than scenario Q, and less fuel is now left for star formation.

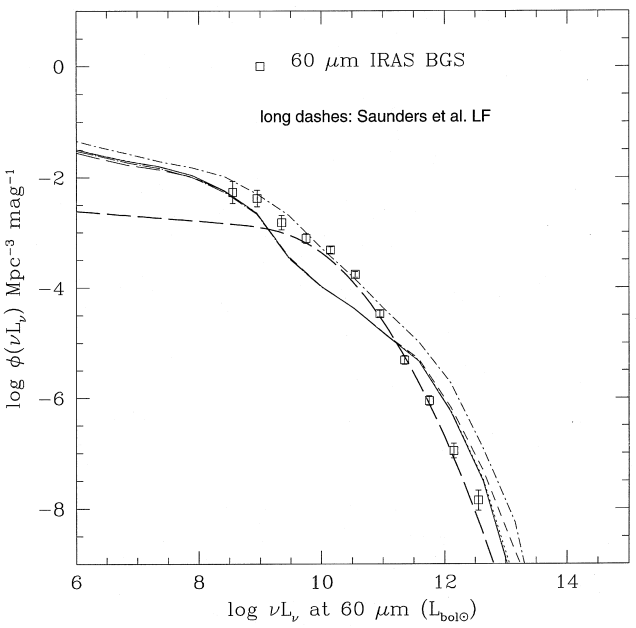

Figure 14. Predicted 60-μm luminosity functions at $z=0$ for the SCDM model with $h=0.5$, $\Omega_0=1$ and $\sigma_8=0.67$. Scenarios Q, A, B, C, D and E are plotted with line codes of Table 1. At $z=0$, scenarios A, B, C, D and E give almost similar results, since the 'burst' mode involves only 4 per cent of the mass. Scenario Q gives a slightly higher luminosity function, since more gas is left to fuel star formation at $z=0$. Squares: observational luminosity function for the *IRAS* Bright Galaxy Sample (Soifer & Neugebauer 1991). Thick long dashes: observational luminosity function from a compilation of various samples (Saunders et al. 1990).

It has been recalled in Section 2.6 that this kind of semi-analytic models predicts too many low-luminosity galaxies in the optical bands at $z=0$ with respect to the observational field luminosity functions (see the references quoted in Section 2.6). As a consequence, the optical luminosity functions are too steep and can be reconciled with the observations by invoking subtle selection effects based on surface brightness. Our model also predicts too many low-luminosity galaxies in the IR, while the discrepancy is somewhat lower than in the blue. The slope is $\phi(L_{\rm IR})\mathrm{d}L_{\rm IR} \propto L_{\rm IR}^{-1.25}\mathrm{d}L_{\rm IR}$. The normalization at the bright end can be improved by a slight decrease (a few tenths dex) of the baryonic density $\Omega_{\rm bar}$, or a slight increase of the baryonic mass-to-luminosity ratios, through the normalization of the 'dark mass' in the IMF.We do not attempt to apply this kind of fine tuning.

5.2 Faint galaxy counts

We hereafter explore the faint counts predicted by using the scenarios proposed in Table 1. Fig. 15 gives the predictions for the *IRAS* 60-μm differential counts normalized to the Euclidean slope. Observational counts from the QMW survey (Rowan-Robinson et al. 1991b), the Faint Source Survey (Lonsdale et al. 1990), the Very Faint Source Survey (Bertin et al. 1997) and the North Ecliptic Pole Region (Hacking & Houck 1987) are superimposed to the predictions. The last survey might be partly affected by a large-scale structure at $z=0.088$ (Ashby et al. 1996). As shown by Bertin et al. (1997), the counts by Gregorich et al. (1995) are contaminated by cirrus. The theoretical curves are *not* renormalized to the bright end of the observed counts. The scenarios involving an increasing fraction of the 'burst' mode predict more galaxies than the no-evolution curve. Scenario D with 15 per cent of ULIGs is rejected by the data. All the other scenarios have a moderate local fraction of ULIGs and are in agreement with the faint counts. Scenario E with an increasing fraction of ULIGs gives an almost flat curve, which is reminiscent of the observational trend. Nevertheless, the rise of the counts below 0.1 Jy, if it is real, is not reproduced. However, our scenarios predict a correct amount of fluctuation, and there is not much space for stronger evolution. More specifically, the counts predict a 60-μm background fluctuation per beam in the Very Faint Source Survey (after removal of $\geq 4\sigma_{\rm tot}=120$ mJy sources) at the level of 14.1 mJy (A), 16.0 mJy (B), 14.3 mJy (C) and 17.0 mJy (E), while the measured 68 per cent quantile is 30.1 ± 1.2 mJy (Bertin et al. 1997). With a 25-mJy rms instrumental noise and 6.5-mJy rms cirrus fluctuations (Gautier et al. 1992), there is still space for a $15.4^{+2.2}_{-2.5}$ mJy fluctuation due to sources, in good agreement with our estimates. Moreover, if the cirrus fluctuations are non-Gaussian, the rms value strongly overestimates the 68 per cent quantile, and can tolerate $16.8^{+2.0}_{-2.3}$ mJy for source fluctuation.

Figs 16 and 17 give the predictions for various wavelengths from 15 μm to 1.4 mm, which correspond to current

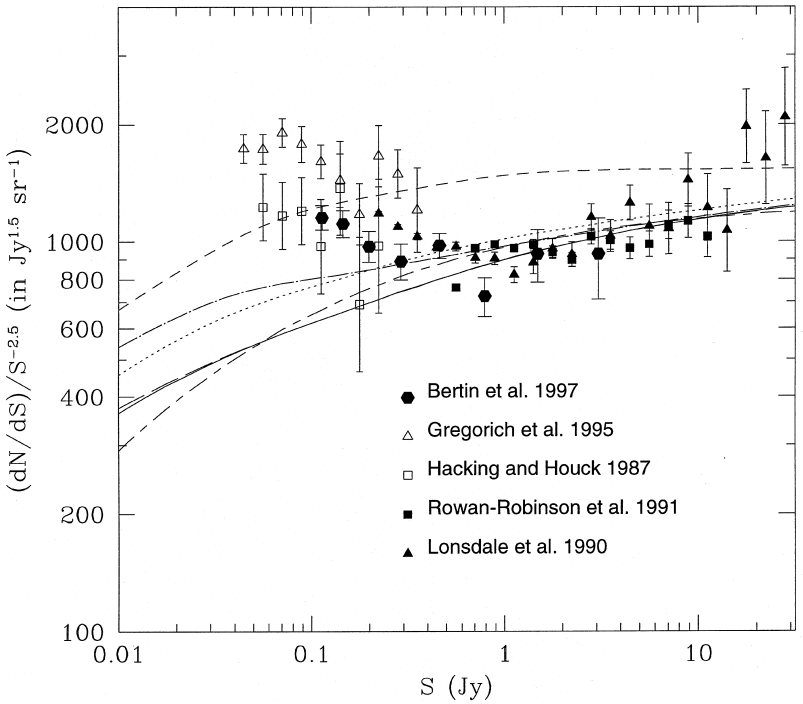

Figure 15. Predictions for differential galaxy counts (normalized to Euclidean counts) at 60 μm. Data are shown for *IRAS* counts at 60 μm. Solid triangles: Faint Source Survey (Lonsdale et al. 1990). Solid squares: QMW survey (Rowan-Robinson et al. 1991b). Solid hexagons: revisited counts in the Very Faint Source Survey (Bertin et al. 1997). Open squares: North Ecliptic Pole Region (Hacking & Houck 1987). These last counts might be affected by the presence of a supercluster. The counts by Gregorich et al. (1995), which are plotted with open triangles, are probably contaminated by cirrus. The no-evolution model (for a cosmology with $h=0.5$, $\Omega_0=1$) is shown with short dashes and long dashes. Scenarios A, B, C, D and E are plotted with line codes of Table 1. Scenario D has too many local ULIGs and should be rejected. Scenario E with an increasing fraction of ULIGs almost reproduces the flat behaviour of the counts.

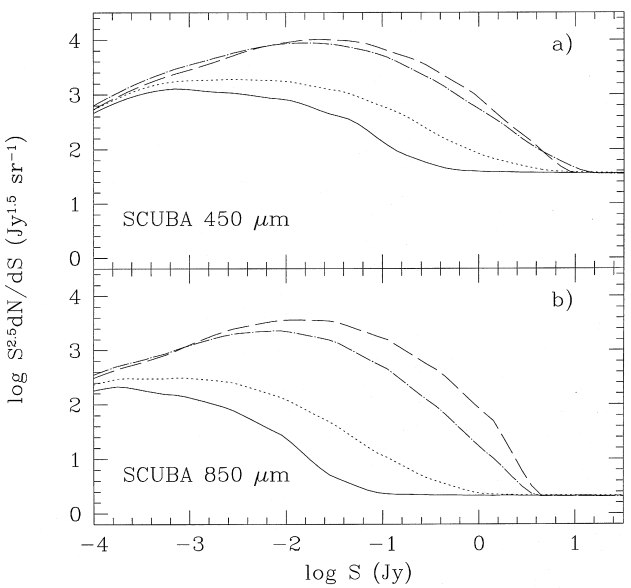

Figure 16. Predictions for differential galaxy counts (normalized to Euclidean counts) at 450 and 850 μm for observations with SCUBA. In contrast with counts at wavelengths smaller than 100 μm, the submm counts are very sensitive to the details of the high-z evolution, because of the shift of the 100-μm bump into the observing bands. Scenarios A, B, C and E are plotted with line codes of Table 1.

and forthcoming instruments. The *IRAS* 60-μm counts are recalled in one of the panels, as well as the *ISO*-HDF 15-μm deep counts (Oliver et al. 1997). Only scenarios A and E are plotted. Clearly, there are three regimes. (i) Nearby galaxies are in the Euclidean zone, giving a count slope $N(>S)\propto S^{-3/2}$. The value of the bright-end normalization at submm wavelengths depends on the choice of the emissivity index m. Since the count rates are very low, it is likely that we shall have to wait for the all-sky survey of *PLANCK* in order to fix the counts at the bright end. (ii) At short wavelengths, the curvature effect and the positive '*k*-correction' produce the bend of the faint counts. (iii) In the submm/mm range, the negative '*k*-correction' produces a bump in the faint counts, which reflects the passage of the 100-μm emission bump into the observing bands.

It appears from Fig. 17 that the *ISO*-HDF counts suggest evolution, but that the predictions are not strongly sensitive to the details of the evolutionary scenario. Guiderdoni et al. (1997) have emphasized the relative degeneracy of the predictions at wavelengths shorter than 100 μm, including the *IRAS* 60-μm and the *ISO* 15-μm counts, and the strong sensitivity of the submm counts to the details of galaxy evolution, which is already apparent for *ISO* observations at 175 μm. Tables 2 and 3 gather the count predictions for the various scenarios of Table 1, and two typical sensitivity levels: 100 mJy, which will be reached for point sources by the *PLANCK* all-sky survey, and which is comparable to the

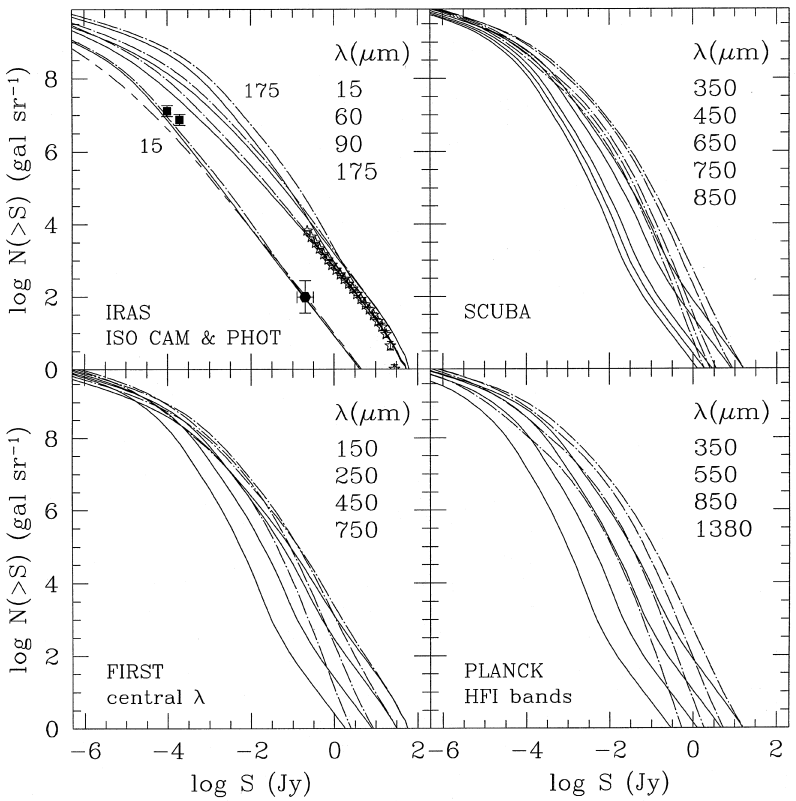

Figure 17. Predictions for number counts at various wavelengths for operating and forthcoming observing facilities and experiments: ISOCAM and ISOPHOT on-board *ISO*, SCUBA, *FIRST* and *PLANCK* High Frequency Instrument. Some of the curves are redundant. The curves correspond to the wavelengths from top to bottom, except in the *IRAS/ISO* Panel where it is from bottom to top. Note that the 15-μm curve only takes into account dust emission (without the stellar component), and the observer-frame fluxes should be considered as lower values beyond $z \sim 1$. The no-evolution prediction at 15 μm (for $h = 0.5$ and $\Omega_0 = 1$) is plotted with short dashes and long dashes. Open stars: *IRAS* at 60 μm (Lonsdale et al. 1990). Solid hexagon: *IRAS* at 12 μm (Rush et al. 1993). Solid squares: *ISO*-HDF counts at 15 μm (Oliver et al. 1997). Scenarios A and E are plotted with line codes as in Table 1.

Table 2. Predictions of galaxy counts in *PLANCK* HFI bands at the 100-mJy level (log number of sources sr^{-1}).

Name	350 μm	550 μm	850 μm	1380 μm
Q	3.97	3.06	2.15	1.18
A	3.93	2.73	1.67	0.71
B	4.41	3.48	2.23	0.83
C	4.95	4.88	4.39	3.15
D	5.04	4.34	3.33	1.77
E	5.08	4.57	3.83	2.39

Table 3. Predictions of galaxy counts in SCUBA and *FIRST* bands at the 10-mJy level (log number of sources sr^{-1}).

Name	350 μm	450 μm	650 μm	750 μm	850 μm
Q	5.66	5.23	4.41	4.09	3.80
A	5.98	5.63	4.73	4.40	3.98
B	6.27	5.99	5.34	5.07	4.75
C	6.80	6.81	6.64	6.52	6.37
D	6.66	6.47	6.01	5.80	5.55
E	6.84	6.75	6.45	6.29	6.09

0.22-Jy level of the *IRAS* 60-μm Faint Source Catalogue, and 10 mJy, which can be reached by deep pencil-beam surveys with SCUBA and *FIRST*. The number counts at 100 and 10 mJy are very sensitive to evolution, and can differ by an order of magnitude at 250 μm, and by more than two orders of magnitude at 850 μm. This explains the discrepancy of the predictions in the literature so far published. Hivon et al. (1998, in preparation) will come back to the detection of submm sources and of the fluctuations they induce. As a conclusion of these predictions, while the *IRAS* data do not yield tight constraints on the evolution of galaxies at $z \geq 0.2$, the forthcoming deep surveys with *ISO* at 175 μm and SCUBA in the atmospheric windows at 450 and 850 μm (for which the array is matched to the instrument optics) will quickly help discriminate between the various scenarios, in the expectation of *PLANCK* and *FIRST*.

5.3 Redshift distributions

Fig. 18 shows the prediction for the redshift distribution corresponding to the spectroscopic follow-up of two *IRAS* samples: the North Ecliptic Pole Region (NEPR) observed by Ashby et al. (1996) with 60-μm fluxes $60 \leq S_{60} \leq 150$ mJy, and the sample of Clements et al. (1996a) for galaxies of the Faint Source Catalogue with $S_{60} \geq 300$ mJy which are 'IR-loud' (IR-to-blue ratios larger than 10). The data of the NEPR are almost complete, and can be directly compared to our predictions. Nevertheless, the first two bins are prob-

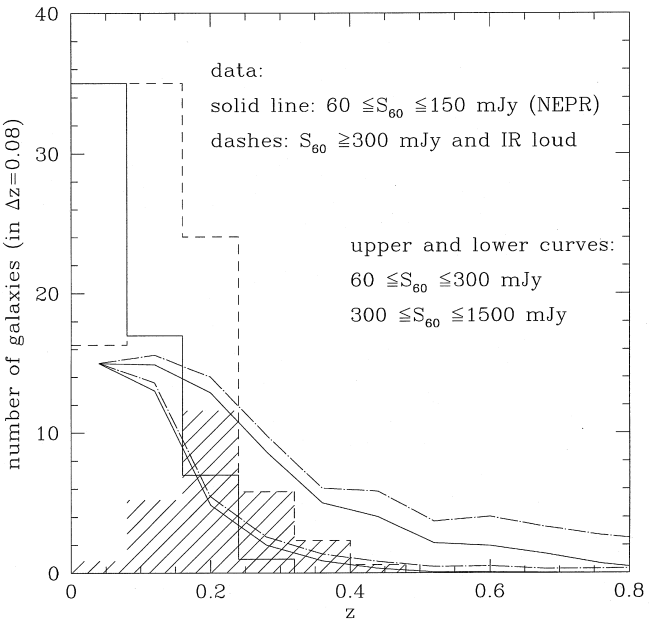

Figure 18. Predicted redshift distribution of the North Ecliptic Pole Region observed by Ashby et al. (1996). The observed galaxies have 60-μm fluxes in the range $60 \leq S_{60} \leq 150$ mJy. The first two bins might be affected by a supercluster. The sample of Clements et al. (1996a) is also plotted for sake of illustration. The reader is referred to this paper for the description of the selection criteria. Roughly, the galaxies have $S_{60} \geq 300$ mJy and are 'IR-loud' (IR-to-blue ratio larger than 10). See text for details. The shaded histogram show the ULIGs of this sample. Scenarios A and E are plotted with line codes of Table 1. Their normalization is relative.

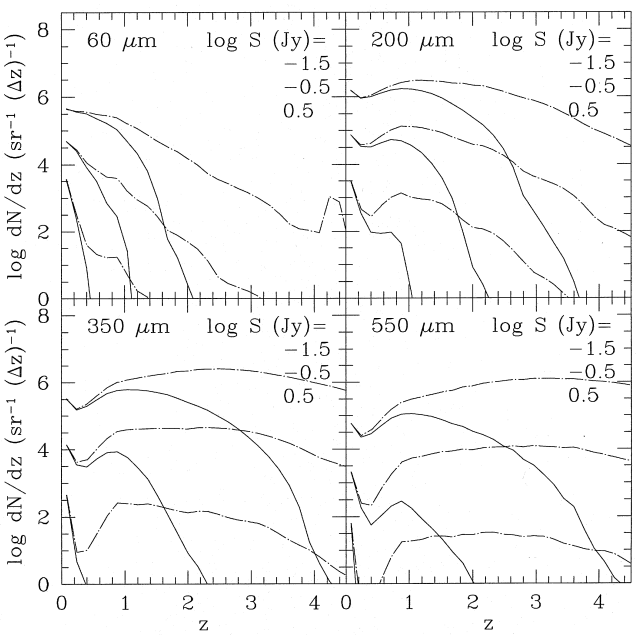

Figure 19. Predictions for redshift distributions at four wavelengths, and in different flux bins. The flux bin widths are $\Delta \log S = 1$, and the central flux values (log S in Jy) are shown in each figure (from top to bottom). Scenarios A and E are plotted with line codes of Table 1.

ably affected by a supercluster at $z = 0.088$. The redshifts of the 'IR-loud' FSC sample have been taken by the authors in order to extract a subsample of ULIGs and not to obtain a complete redshift survey. The histogram given for the galaxies which are not ULIGs (144 sources) has been roughly rescaled to take into account the number of sources not quoted in their appendix because they already have redshifts in the literature. The shaded histogram shows their 91 ULIGs. Then the histogram is renormalized in order to peak at the same relative level as the NEPR. The sample has only a 60 per cent completeness. In general, the scenarios seem to predict more galaxies at high z than in the NEPR sample. The 'IR-loud' FSC sample plotted here suffers from problems of overall normalization and incompleteness, but it signals the presence of galaxies at $z \geq 0.2$. The difference between the redshift distributions for scenarios E and A gives the fraction of ULIGs in scenario E (there are no ULIGs in scenario A). The distribution of ULIGs with z seems to be much flatter than the observed peak in the 'IR-loud' FSC sample. However, it is difficult to assess the level of discrepancy with a 60 per cent incompleteness. Clearly, the redshift follow-up of deep, IR-selected samples is still an ongoing project, and it will bring crucial information on the nature of the sources.

Fig. 19 shows predictions for the redshift distributions at 60, 200, 350 and 550 μm, corresponding to various flux depths. Scenarios A and E (as well as B, C and D not plotted here) give different predictions at $z \geq 1$. For scenario A, the redshift distributions at the 10-mJy flux level peak at $z \sim 1$, with a high-z tail encompassing 90 per cent of the sources at $z \sim 2.5$ to 3. Scenario E has galaxies at still higher z. In contrast with the *IRAS* samples at 60 μm which, at the 100 mJy flux level, probe only the Universe at $z \sim 0.2$, the future spectroscopic follow-up of submm observations at the 10-mJy level should be able to explore the IR/submm evolution of galaxies at $z \geq 1$. Finally, Fig. 20 shows the contribution of sources fainter than S to the background value at 60, 200 and 550 μm. The 10-mJy level which will be reachable by the forthcoming submm observations will allow the surveys to begin 'breaking' the CIB into discrete units.

6 DISCUSSION AND CONCLUSIONS

We have used a simple semi-analytic model of galaxy formation to derive the IR/submm statistical properties of galaxies: luminosity function, faint galaxy counts, redshift distributions and the diffuse background. The model shares many common features with previous semi-analytic works focusing upon the optical properties of galaxies. (i) The collapse of the perturbations is described by the classical top-hat model under the assumptions of homogeneity and sphericity; in this simple version, we used the peaks formalism to compute the formation rate of haloes. (ii) The dissipative cooling and collapse is introduced, with the usual 'overcooling' problem, which can be partly suppressed by introducing feedback due to overall reionization and galactic winds triggered by SNe. (iii) Star formation is proportional to the ratio of the gas content to the dynamical time-scale of the galaxies. (iv) Stellar evolution is explicitly implemented.

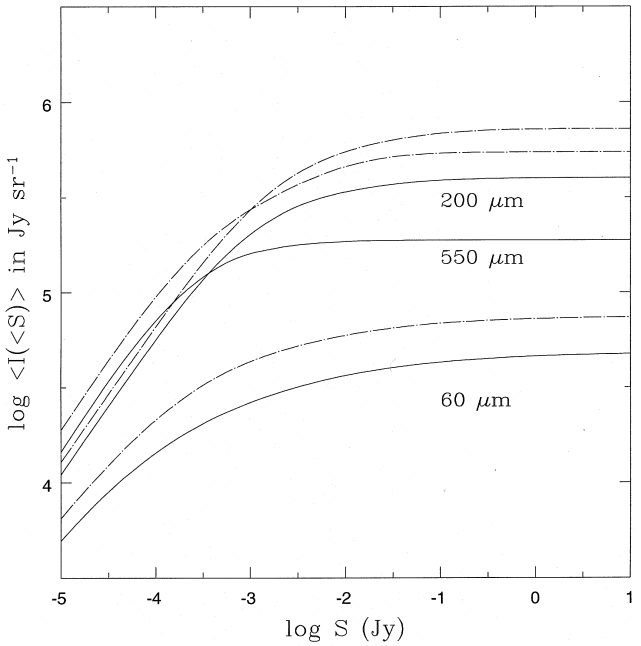

Figure 20. Contribution of sources fainter than S to the background value at 60, 200 and 550 μm. Scenarios A and E are plotted with line codes of Table 1.

In order to make specific predictions for the IR/submm wavelength range, this model includes the following assumptions.

(i) An average optical depth of the discs is implemented and scales as the relative gas content and gas metallicity (estimated through the assumption of instant recycling approximation); no evolution of the dust composition is considered; the variation of the extinction curve with metallicity is based on an interpolation of the Milky Way and the Magellanic Clouds which gives an extinction proportional to $Z^{1.6}$.

(ii) A simple 'slab' geometry is assumed where dust and stars are mixed with equal height-scales.

(iii) Finally, the dust emission spectrum scales with the bolometric IR luminosity, following the observational relationship of *IRAS* colours with luminosities. Such a dependence is obtained by changing the abundance of three components: PAH, very small grains and big grains (and the temperature of the big grains).

We introduced two modes of star formation. In the 'quiescent' mode, the distribution of the characteristic time-scales t_* for star formation peaks at 3 Gyr, and ranges from 0.3 to 30 Gyr. In the 'burst' mode, the distribution of t_* peaks at 0.30 Gyr, and ranges from 0.03 to 3 Gyr. The 'quiescent' mode is unable to reproduce the rapid evolution of the cosmic SFR and gas densities. The steep decline of the SFR and gas content since $z=2$ can be accommodated by assuming an increasing fraction of mass involved in the 'burst' mode. Since one knows that the fraction of peculiar objects with signs of interaction/merging increases with the depth of the survey, we suspect that the bursting behaviour of the CFRS and HDF galaxies is due to interactions, and we introduce a phenomenological z dependence fitting the evolution of the pair rates. Since LIGs and ULIGs are respectively interacting and merging systems, it is reasonable to estimate that, reciprocally, CFRS and HDF galaxies with peculiar morphologies should emit in the IR. For these 'mild starburts' and 'luminous IR/UV galaxies', we assume a conservative range of IR-to-blue luminosity ratios $0.06 \leq L_{IR}/\lambda_B L_B \leq 4$ computed from our standard assumptions on average optical thickness and geometry. Finally, in order to reproduce the bright end of IR galaxies with $L_{IR}/\lambda_B L_B \geq 10$, we also introduced a population of heavily extinguished galaxies with massive star formation, similar to ULIGs.

With these ingredients, we designed a family of evolutionary scenarios which fit the local overall energy budget and its evolution to $z \sim 1$. These scenarios also fit the COB estimate computed from faint galaxy counts, and are consistent with the observational range for the CIB. So we feel confident that we roughly reproduce the local energy budgt as well as a plausible range for the integrated budget along the line of sight. The scenarios predict UV and IR emissions strongly differing at high z. With the same SFR history, different UV fluxes can be obtained with different extinctions and IMF. In some of the scenarios, the UV fluxes at $z=4$ fit the current measurements (or lower values) of Madau et al. (1996), but with 10 times more SFR than deduced *under the assumption of no extinction.* Such a factor of 10, which includes the contribution of heavily extinguished ULIGs, is larger than the factor of 3 corresponding to the correction for extinction derived by Pettini et al. (1998) for the HDF galaxies with Lyman-continuum drop-outs. This quantifies the strong warning that the deduction of the SFR density from UV fluxes misses the optically dark side of galaxy formation.

This family of scenarios was obtained within the context of the same cosmological model, with similar prescriptions for dissipative and non-dissipative collapses, star formation and feedback. The changes only affect the efficiency of star formation on a dynamical time-scale (the β parameter), the IMF (Salpeter or only massive stars), and the extinction (average extinction with 'slab' geometry, or strong, 'screen'-like extinction). We saw the extreme sensitivity of the predictions to the parameter choice for this poorly constrained astrophysics.

The scenarios are consistent with *IRAS* data. They give similar predictions for the *IRAS* 60-μm luminosity function and faint counts, provided the local fraction of ULIGs is lower than a few per cent. They are in rough agreement with the redshift surveys of *IRAS* samples, in spite of some uncertainty in the data. By construction, the IR spectra also fit the correlation of IR colours with total IR luminosity in the Bright Galaxy Sample. The selected scenarios are consistent with the $\pm 1\sigma$ range for the observed CIB, and they are used to 'disentangle' the background into faint galaxy counts. This CIB is the first 'post-*IRAS*' observation which helps constraining the high-z evolution of galaxies in the IR/submm and the energy budget integrated along the line of sight, before *ISO* results. In contrast with the counts at FIR wavelengths which are rather degenerate, the submm counts are very sensitive to the details of the evolutionary scenarios. Thus our study illustrates the importance of the submm range to constrain the evolution of the energy budget of galaxies. As emphasized by Guiderdoni et al. (1997), our understanding of the formation and evolution of

galaxies is so far based entirely on surveys in the UV/visible window. We are missing the part of star/galaxy formation hidden by dust. We need to open a second window in the IR/submm, which is being explored by *ISO* and SCUBA, and will be extensively studied by forthcoming telescopes and satellites such as *SIRTF*, SOFIA, *FIRST* and *PLANCK*.

There are clearly many approximations and shortcomings in our approach, which could be listed as a research programme for forthcoming papers. (i) We need to implement the astrophysical processes in a code which explicitly follows the merging history trees of haloes and galaxies. This code would have to include the various aspects of interaction between galaxies, and to explain why the interaction rate strongly declined since $z=1$. It would also have to include the effect of interactions on the SFR. (ii) The modelling of the IR emission could take into account the evolution of dust properties with chemical abundances, as well as more sophisticated transfer. (iii) The global energy budget of galaxies has to be addressed by fitting the faint galaxy counts in the UV/visible and *K*, as well as the forthcoming NIR counts from *ISO*, in particular at 15 μm. First results are already given here, and suggest an amount of evolution which is consistent with our predictions. (iv) The strong evolution of the comoving SFR density has consequences on the gas and heavy-element abundances. The heavy elements made by the high SFRs are to be found in the stars, the cold gas, or the hot gas of the intergalactic medium (IGM). If the SFR turned out to be much higher than that determined, for instance, by Madau et al. (1996), a significant fraction of the heavy elements should be present in the IGM. The amount of elements synthesized in bursts would still be higher if the IMF were top-heavy, as in the simple model of ULIGs which is used here. According to Mushotzky & Loewenstein (1997), the absence of evolution of the iron content of clusters at $z\sim0.3$ is a first evidence that the global metal production was 2–5 times higher than inferred from the UVB drop-out technique.

Despite the limitations listed above, this paper provides the first predictions of the IR luminosity function, IR/submm galaxy counts, redshift distribution and diffuse background, obtained from a semi-analytic model of galaxy formation and evolution which takes into account the main physical processes from the collapse of the density fluctuations to the absorption of UV and visible star light by dust and the re-emission in the IR/submm range. The predictions of this new model are consistent with the dynamical process of continuous galaxy formation predicted by the hierarchical growth of structures in a SCDM universe, and represent a significant progress with respect to previous phenomenological models designed to make predictions in the IR/submm.

Tables giving the faint counts and redshift distributions at various wavelengths between 15 μm and 2 mm are available by anonymous ftp at ftp.iap.fr in the directory /pub/from_users/guider/fir, and on the Web node of the Institut d'Astrophysique de Paris at
http://www.iap.fr/users/guider/fir.html.

ACKNOWLEDGMENTS

We are pleased to thank Stéphane Charlot, Dave Clements, François-Xavier Désert, David Elbaz, Michael Fall, Karl Glazebrook and Jean-Loup Puget for their comments and suggestions.

REFERENCES

Abraham R. G., Tanvir N. R., Santiago B. X., Ellis R. S., Glazebrook K., van den Bergh S., 1996, MNRAS, 279, L47
Andreani P., Franceschini A., 1992, A&A, 260, 89
Andreani P., Franceschini A., 1996, MNRAS, 283, 85
Ashby M. L. N., Hacking P. B., Houck J. R., Soifer B. T., Weisstein E. W., 1996, ApJ, 456, 428
Bardeen J. M., Bond J. R., Kaiser N., Szalay A. S., 1986, ApJ, 304, 15
Barnes J., Efstathiou G., 1987, ApJ, 319, 575
Baugh C. M., Cole S., Frenk C. S., 1996a, MNRAS, 283, L15
Baugh C. M., Cole S., Frenk C. S., 1996b, MNRAS, 283, 1361
Baugh C. M., Cole S., Frenk C. S., Lacey C. G., 1998, ApJ, in press
Beichman C. A., Helou G., 1991, ApJ, 370, L1
Bertin E., Dennefeld M., Moshir M., 1997, A&A, 323, 685
Blain A. W., Longair M. S., 1993a, MNRAS, 264, 509
Blain A. W., Longair M. S., 1993b, MNRAS, 265, L21
Blanchard A., Valls-Gabaud D., Mamon G., 1992, A&A, 264, 365
Bond J. R., 1988, in Unruh W. G., Semenoff G. W., eds, NATO ASI Series, The Early Universe. Reidel, Dordrecht, p. 322
Bosma A., 1991, AJ, 86, 1825
Briggs F. H., Rao S., 1993, ApJ, 417, 494
Burkey J. M., Keel W. C., Windhorst R. A., Franklin B. E., 1994, ApJ, 429, L13
Carico D. P., Keene J., Soifer B. T., Neugebauer G., 1992, PASP, 104, 1086
Carlberg R. G., 1990, ApJ, 359, L1
Carlberg R. G., Pritchet C. J., Infante L., 1993, ApJ, 435, 540
Charbonnel C., Meynet G., Maeder A., Schaerer D., 1996, A&AS, 115, 339
Chini R., Krügel E., 1993, A&A, 279, 385
Chini R., Kreysa E., Krügel E., Mezger P. G., 1986, A&A, 166, L8
Clements D. L., Andreani P., Chase S. T., 1993, MNRAS, 261, 299
Clements D. L., Sutherland W. J., Saunders W., Efstathiou G. P., McMahon R. G., Maddox S., Rowan-Robinson M., 1996a, MNRAS, 279, 459
Clements D. L., Sutherland W. J., McMahon W. J., Saunders R. G., 1996b, MNRAS, 279, 477
Cole S., 1991, ApJ, 367, 45
Cole S., Aragón-Salamanca A., Frenk C. S., Navarro J. F., Zepf S. E., 1994, MNRAS, 271, 781
Connolly A. J., Szalay A. S., Dickinson M., SubbaRao M. U., Brunner R. J., 1997, ApJ, 486, L11
Cowie L. L., Songaila A., Hu E. M., Cohen J. D., 1996, AJ, 112, 839
Dekel A., Silk J., 1986, ApJ, 303, 39
Désert F. X., Boulanger F., Puget J. L., 1990, A&A, 237, 215
Disney M., Davies J., Philipps S., 1989, MNRAS, 239, 939
Draine B. T., Lee H. M., 1984, ApJ, 285, 89
Dwek E., Városi F., 1996, in Dwek E., ed., Unveiling the Cosmic Infrared Background. AIP Conference Proceedings 348
Eales S. A., Edmunds M. G., 1996, MNRAS, 280, 1167
Eales S. A., Edmunds M. G., 1997, MNRAS, 286, 732
Eales S. A., Wynn-Williams C. G., Duncan W. D., 1989, ApJ, 339, 859
Efstathiou G., 1992, MNRAS, 256, 43P
Efstathiou G., Frenk C. S., White S. D. M., Davis M., 1988, MNRAS, 235, 715
Eisenhardt P., Armus L., Hogg D. W., Soifer B. T., Neugebauer G., Werner M. W., 1996, ApJ, 461, 72

Ellis R. S., Colless M., Broadhurst T. J., Heyl J. S., Glazebrook K., 1996, MNRAS, 280, 235
Evrard A. E., 1989, ApJ, 341, 26
Fall S. M., Efstathiou G., 1980, MNRAS, 193, 189
Fall S. M., Charlot S., Pei Y. C., 1996, ApJ, 464, L43
Franceschini A., Andreani P., 1995, ApJ, 440, L5
Franceschini A., Toffolatti L., Mazzei P., Danese L., De Zotti G., 1991, A&AS, 89, 285
Franceschini A., Mazzei P., De Zotti G., Danese L., 1994, ApJ, 427, 140
Gautier T. N., III, Boulanger F., Perault M., Puget J. L., 1992, AJ, 103, 1313
Gregorich D. T., Neugebauer G., Soifer B. T., Gunn J. E., Herter T. L., 1995, AJ, 110, 259
Griffiths R. E., Ratnatunga K. U., Neuschaefer L. W., Casertano S., Im M., 1994, ApJ, 437, 67
Guiderdoni B., 1987, A&A, 172, 27
Guiderdoni B., Rocca-Volmerange B., 1987, A&A, 186, 1
Guiderdoni B., Rocca-Volmerange B., 1988, A&AS, 74, 185
Guiderdoni B., Hivon E., Bouchet F. R., Maffei B., Gispert R., 1996, in Dwek E., ed., Unveiling the Cosmic Infrared Background. AIP Conference Proceedings 348
Guiderdoni B., Bouchet F. R., Puget J. L., Lagache G., Hivon E., 1997, Nat, 390, 257
Hacking P., Houck J. R., 1987, ApJS, 63, 311
Hacking P. B., Soifer B. T., 1991, ApJ, 367, L49
Haehnelt M. G., Rees M. J., 1993, MNRAS, 263, 168
Hauser M. G., 1995, in Kafatos M., Kondo Y., eds, Proc. IAU Symp. 168, Examining the Big Bang and Diffuse Background Radiations. Kluwer, Dordrecht, p. 99
Helou G., Soifer B. T., Rowan-Robinson M., 1985, ApJ, 298, L7
Heyl J. S., Cole S., Frenk C. S., Navarro J. F., 1995, MNRAS, 274, 755
Hughes D. H., Dunlop J. S., Rawlings S., 1997, MNRAS, 289, 766
Kauffmann G. A. M., 1995, MNRAS, 274, 161
Kauffmann G. A. M., 1996, MNRAS, 281, 487
Kauffmann G. A. M., White S. D. M., Guiderdoni B., 1992, MNRAS, 264, 201
Kauffmann G. A. M., Guiderdoni B., White S. D. M., 1994, MNRAS, 267, 981
Kauffmann G. A. M., Charlot S., White S. D. M., 1996, MNRAS, 283, L117
Kennicutt R. C., 1989, ApJ, 344, 685
Kennicutt R. C., 1998, in Guiderdoni B., Kembhavi A., eds, Starbursts: Triggers, Nature and Evolution. Editions de Physique/Springer-Verlag, in press
Kennicutt R. C., Tamblyn P., Congdon C. W., 1994, ApJ, 435, 22
Lacey C., Silk J., 1991, ApJ, 381, 14
Lacey C., Guiderdoni B., Rocca-Volmerange B., Silk J., 1993, ApJ, 402, 15
Lanzetta K. M., Wolfe A. M., Turnshek D. A., 1995, ApJ, 440, 435
Lilly S. J., Tresse L., Hammer F., Crampton D., Le Fèvre O., 1995, ApJ, 455, 108
Lilly S. J., Le Fèvre O., Hammer F., Crampton D., 1996, ApJ, 460, l1
Lonsdale C. J., 1996, in Dwek E., ed., Unveiling the Cosmic Infrared Background. AIP Conference Proceedings 348
Lonsdale C. J., Hacking P. B., Conrow T. P., Rowan-Robinson M., 1990, ApJ, 358, 60
Loveday J., Peterson B. A., Efstathiou G., Maddox S. J., 1992, ApJ, 390, 79
Madau P., Ferguson H. C., Dickinson M. E., Giavalisco M., Steidel C. C., Fruchter A., 1996, MNRAS, 283, 1388
Maffei B., 1994, PhD dissertation, Univ. Paris VII
Marzke R. O., Huchra J. P., Geller M. J., 1994, ApJ, 428, 43
Mathis J. S., Mezger P. G., Panagia N., 1983, A&A, 128, 212
McGaugh S. S., 1994, Nat, 367, 538
Mushotzky R. F., Loewenstein M., 1997, ApJ, 481, L63
Natarajan P., Pettini M., 1997, MNRAS, 291, L28
Natta A., Panagia N., 1984, ApJ, 287, 228
Navarro J. F., White S. D. M., 1993, MNRAS, 265, 271
Oliver S. J., Rowan-Robinson M., Saunders W., 1992, MNRAS, 256, 15P
Oliver S. J., Goldschmidt P., Franceschini A., Sergeant S. B. G., Efstathiou A., 1997, MNRAS, 289, 471
Pearson C., Rowan-Robinson M., 1996, MNRAS, 283, 174
Pei Y. C., Fall S. M., 1995, ApJ, 454, 69
Pettini M., Steidel C. S., Dickinson M., Kellogg M., Giavalisco M., Adelberger K. L., 1998, in Shull J. M., Woodward C. E., Thronson H., eds, ASP Conf. Ser., Origins, in press
Puget J. L., Abergel A., Bernard J. P., Boulanger F., Burton W. B., Désert F. X., Hartmann D., 1996, A&A, 308, L5
Reach W. T., Dwek E., Fixsen D. J., Hewagama T., Mather J. C., 1995, ApJ, 451, 188
Rice W., Lonsdale C. J., Soifer B. T., Neugebauer G., Kopan E. L., Lloyd L. A., de Jong T., Habing H. J., 1988, ApJS, 68, 91
Rocca-Volmerange B., Guiderdoni B., 1988, A&AS, 75, 93
Rowan-Robinson M., 1992, MNRAS, 258, 787
Rowan-Robinson M., Broadhurst T., Lawrence A., McMahon R. G., Lonsdale C. J., 1991a, Nat, 351, 719
Rowan-Robinson M., Saunders W., Lawrence A., Leech K., 1991b, MNRAS, 253, 485
Rush B., Malkan M., Spinoglio L., 1993, ApJS, 89, 1
Sanders D. B., Mirabel I. F., 1996, ARA&A, 34, 749
Saunders W., Rowan-Robinson M., Lawrence A., Efstathiou G., Kaiser N., Ellis R. S., Frenk C. S., 1990, MNRAS, 242, 318
Sawicki M. J., Lin H., Yee H. K. C., 1997, AJ, 113, 1
Schaeffer R., Silk J., 1985, ApJ, 292, 319
Schaller G., Schaerer D., Meynet G., Maeder A., 1992, A&AS, 96, 269
Smith B. J., Kleinmann S. G., Huchra J. P., Low F. J., 1987, ApJ, 318, 161
Soifer B. T., Neugebauer G., 1991, AJ, 101, 354
Soifer B. T., Sanders D. B., Madau B. F., Neugebauer G., Danielson G. E., Elias J. H., Lonsdale C. J., Rice W. L., 1987, ApJ, 320, 238
Stark A. A., Davidson J. A., Harper D. A., Pernic R., Loewenstein R., Platt S., Engargiola G., Casem S., 1989, ApJ, 337, 650
Steidel C. C., Giavalisco M., Pettini M., Dickinson M., Adelberger K. L., 1996, ApJ, 462, L17
Storrie-Lombardi L. J., McMahon R. G., Irwin M. J., 1996, MNRAS, 283, L79
Thornton K., Gaudlitz M., Janka H. T., Steinmetz M., 1998, ApJ, in press
Treyer M., Silk J., 1993, ApJ, 408, L1
Wang B., 1991a, ApJ, 374, 456
Wang B., 1991b, ApJ, 374, 465
Weedman D. W., 1990, in Leitherer C., Walborn N. R., Hackman T. M., Norman C. A., eds, Massive Stars in Starbursts. Cambridge Univ. Press, Cambridge, p. 317
White S. D. M., Rees M. J., 1978, MNRAS, 183, 341
White S. D. M., Frenk C. S., 1991, ApJ, 379, 52
Williams R. E., Blacker B., Dickinson M., Van Dyke Dixon W., Ferguson H. C., 1996, AJ, 112, 1335
Zepf S. E., Koo D. C., 1989, ApJ, 337, 34
Zurek W. H., Quinn P. J., Salmon J. K., 1988, ApJ, 330, 519

APPENDIX A: MASS DISTRIBUTION OF COLLAPSED HALOES

The initial, linear perturbation is assumed to be spherical and homogeneous. This is the so-called 'top-hat' model, which has the friendly property of being entirely defined by

two parameters – for instance, the size R and density contrast $(\delta\rho/\rho)_{z=0}\equiv\delta_0$ which are the linearly extrapolated values at $z=0$, or, equivalently, the mass M and collapse redshift $z_{\rm coll}$. If ρ_0 is the current mass density of the Universe, we have $M=(4\pi/3)R^3\rho_0$.

The linearly extrapolated density contrast, and the ratio of the radius of maximal expansion $r_{\rm m}$ to the linearly extrapolated size R, can be respectively computed as functions of the redshift of collapse:

$$\delta_0=\delta_0[1+z_{\rm coll}],\qquad r_{\rm m}/R=r_{\rm m}/R[1+z_{\rm coll}]. \tag{A1}$$

For instance, if $\Omega_0=1$, then $\delta_0=\delta_{\rm c}(1+z_{\rm coll})$ with $\delta_{\rm c}=1.68$, and $r_{\rm m}/R=(3/5\delta_0)$. After collapse and violent relaxation, a mean potential forms and the virialized halo ends as a singular, isothermal sphere truncated at 'virial radius' $r_{\rm V}=r_{\rm m}/2$. If we define a 'circular velocity' as $V_{\rm c}\equiv(GM/r_{\rm V})^{1/2}$, the density profile of the relaxed halo at $r\le r_{\rm V}$ is

$$\rho_{\rm H}(r)=\frac{V_{\rm c}^2}{4\pi G r^2}, \tag{A2}$$

and the mass included within radius r is simply $M(<r)=Mr/r_{\rm V}$. For instance, if $\Omega_0=1$, the virial radius (in Mpc) and the circular velocity (in km s^{-1}) are

$$r_{\rm V}=0.17\left(\frac{M}{10^{12}\ {\rm M}_\odot}\right)^{1/3}(1+z_{\rm coll})^{-1}h^{-2/3}, \tag{A3}$$

$$V_{\rm c}=160\left(\frac{M}{10^{12}\ {\rm M}_\odot}\right)^{1/3}(1+z_{\rm coll})^{1/2}h^{1/3}. \tag{A4}$$

We hereafter take $h\equiv H_0/(100\ {\rm km\ s^{-1}\ Mpc^{-1}})$. Finally, the virial temperature of the baryonic gas is

$$T_{\rm V}=\frac{1}{2}\frac{\mu m_{\rm p}}{k}V_{\rm c}^2=35.9\left(\frac{V_{\rm c}}{\rm km\ s^{-1}}\right)^2\ {\rm K}, \tag{A5}$$

$m_{\rm p}$ is the mass of the proton, and the mean molecular weight $\mu=0.59$ corresponds to ionized gas with respective H and He mass fractions $X=0.75$ and $Y=0.25$.

Then we compute the mass distribution of collapsed haloes from the peaks formalism (Bardeen et al. 1986), as in Lacey & Silk (1991) and Lacey et al. (1993). We start from the power spectrum of the linear fluctuations $P(k)$ which is normalized by σ_8, the variance at a *top-hat* smoothing radius $R=8\ h^{-1}$ Mpc. The peaks formalism uses momenta of the power spectrum with Gaussian smoothing on radius $R_{\rm G}$. The mass included within such a radius is $M=(2\pi)^{3/2}R_{\rm G}^3\rho_0$. So the relation between the Gaussian radius $R_{\rm G}$ and the top-hat radius R including mass M is simply $R_{\rm G}=0.64R$. These momenta are computed from

$$\sigma_{\rm m}(R_{\rm G})^2=\frac{1}{8\pi^3}\int k^{2m}P(k)|W_k(kR_{\rm G})|^2 4\pi k^2{\rm d}k, \tag{A6}$$

where $W_k(y)=\exp(-y)$ is the Fourier transform of the Gaussian filtering function

$$W(x)=\frac{1}{(2\pi R_{\rm G}^2)^{3/2}}\exp\left(-\frac{|x|^2}{2R_{\rm G}^2}\right). \tag{A7}$$

The (comoving) number density distribution of peaks $\nu\equiv\delta_{0{\rm G}}/\sigma_0(R_{\rm G})$, in which $\delta_{0{\rm G}}$ is smoothed on the Gaussian scale $R_{\rm G}$, is

$$\frac{\partial n_{\rm pk}(R_{\rm G})}{\partial\nu}\,{\rm d}\nu=n_{\rm pk}(R_{\rm G})P(\nu,R_{\rm G}){\rm d}\nu, \tag{A8}$$

with

$$n_{\rm pk}(R_{\rm G})=\frac{c_\infty}{4\pi^2R_*^3}, \tag{A9}$$

$$P(\nu,R_{\rm G})=\frac{1}{c_\infty}\exp\left(-\frac{\nu^2}{2}G(\gamma,\gamma\nu)\right), \tag{A10}$$

such as $\int P(\nu,R_{\rm G}){\rm d}\nu=1$. The functions R_* and γ are computed as

$$R_*(R_{\rm G})\equiv\sqrt{3}\,\frac{\sigma_1(R_{\rm G})}{\sigma_2(R_{\rm G})},\qquad \gamma(R_{\rm G})\equiv\frac{\sigma_1^2(R_{\rm G})}{\sigma_0(R_{\rm G})\sigma_2(R_{\rm G})}. \tag{A11}$$

The constant $c_\infty=0.6397$, and an analytic fit of the function $G(\gamma,\omega)$ is given by equations (4.4) and (4.5) of Bardeen et al. (1986). If $P(k)\propto k^n$, it is easy to check that $\gamma(R_{\rm G})$ does not depend on $R_{\rm G}$, and that $R_*(R_{\rm G})\propto R_{\rm G}$. For $\Omega_0=1$, $h=0.5$, and the CDM power spectrum with $-3\le n\le 1$, we have slow variations: $0.55<\gamma(R_{\rm G})\le 0.8$ and $1.05\le R_*(R_{\rm G})/R_{\rm G}\le 1.5$ for $0.1\le R_{\rm G}\le 100$ Mpc.

At that stage, we do not have the number density distribution of peaks per bin of density contrast *and* radius. For that purpose, we have to introduce, as in Lacey & Silk (1991), a suggestion by Bond (1988), who interprets equation (A9) as the total number density of peaks $n_{\rm pk}(>R_{\rm G})$ at scale $>R_{\rm G}$. By derivating equation (A8), it is easy to get:

$$\frac{\partial^2 n_{\rm pk}}{\partial R_{\rm G}\partial\nu}\,{\rm d}R_{\rm G}{\rm d}\nu=-\frac{3\ {\rm d}\ln R_*}{R_{\rm G}\ {\rm d}\ln R_{\rm G}}\,n_{\rm pk}(R_{\rm G})P(\nu,R_{\rm G}){\rm d}R_{\rm G}{\rm d}\nu. \tag{A12}$$

We neglect the slow variation of $\gamma(R_{\rm G})$ with $R_{\rm G}$. This is the number density of *all* peaks. We now need to count the peaks over a certain threshold $\nu_{\rm th}$ for collapse, and we get the formation rate of haloes:

$$\frac{\partial^2 n_{\rm for}}{\partial R_{\rm G}\partial\nu_{\rm th}}\,{\rm d}R_{\rm G}{\rm d}\nu_{\rm th}=\frac{\partial}{\partial\nu_{\rm th}}\left(\int_{\nu_{\rm th}}^{\infty}\frac{\partial^2 n_{\rm pk}}{\partial R_{\rm G}\partial\nu}\,{\rm d}\nu\right){\rm d}R_{\rm G}{\rm d}\nu_{\rm th}. \tag{A13}$$

After a change of variables, we get the halo formation rate, since $\nu_{\rm th}\equiv\delta_{0{\rm G},{\rm th}}[1+z_{\rm coll}]/\sigma_0(R_{\rm G})$:

$$\frac{\partial^2 n_{\rm for}}{\partial\ \ln\ M\partial(1+z_{\rm coll})}=-n_{\rm pk}(>R_{\rm G})\,\frac{{\rm d}\ln R_*}{{\rm d}\ln R_{\rm G}}\,P(\nu_{\rm th},R_{\rm G})$$
$$\times\frac{1}{\sigma_0(R_{\rm G})}\,\frac{{\rm d}\delta_{0{\rm G},{\rm th}}[1+z_{\rm coll}]}{{\rm d}(1+z_{\rm coll})}. \tag{A14}$$

In order to link the Gaussian smoothing to the top-hat formalism, we take $R_{\rm G}=0.64R$ and $\delta_{0{\rm G},{\rm th}}\equiv\delta_0\sigma_0(R)/\sigma_0(R_{\rm G})$. The total number of collapsed peaks at redshift $(1+z)$ is obtained by integrating equation (A14) on all redshifts larger than $(1+z)$.

The number density increases continuously with time, at all masses, contrary to what is found from the Press–

Schechter formalism. The peaks formalism follows the collapse of *all* peaks, and counts high peaks at well as the broader, shallower peaks in which these high peaks are included. This so-called 'cloud-in-cloud' problem results in a possible overestimate of the total number of galaxies. As a matter of fact, the total number density of peaks at the low-mass end of the mass function varies as M^{-2}, and the total mass density grows logarithmically with the lower mass cut-off. Anyhow, since other astrophysical phenomena will act to 'suppress' galaxy formation in low-mass haloes, we find that this slow divergence is not too serious a problem.

Finally, we do not explicitly include the merging of galaxies in merging haloes. In our crude modelling, new galaxies form at each generation of peak collapse.This model could be fitted to the description of 'active' objects such as luminous galaxies seen in the IR. Such a simplifying assumption is very similar to that of Haehnelt & Rees (1993), who modelled QSO formation in each generation of halo formation. The issue of merging should be explicitly addressed by making Monte Carlo realizations of the halo merging history trees and monitoring the merging of galaxies in merged haloes, for instance with the dynamical friction time-scale (Kauffmann et al. 1993; Cole et al. 1994, and following works). Such studies show that the galaxy merging rate is relatively low, and that the resulting mass and luminosity functions do not differ significantly from those computed with cruder assumptions. More precisely, galaxy merging seems to be sufficient to make the 10 per cent fraction of giant galaxies which are elliptical, but does not produce a significant change in the slope of the luminosity function at faint magnitudes. The implementation of the astrophysics hereafter described into this type of code is clearly one of the next steps of our programme. Nevertheless, it is worthwhile to note that only merging following the slow process of dynamical friction has been currently modelled. Two-body encounters and tidal interactions, which trigger starburst activity as it clearly appears from observational evidence, are not modelled yet in the current Monte Carlo codes.